ACS APPLIED MATERIALS & INTERFACES

Research Article

Cite This: ACS Appl. Mater. Interfaces 2019, 11, 10505−10519

www.acsami.org

Combinational Effects of Active Targeting, Shape, and Enhanced Permeability and Retention for Cancer Theranostic Nanocarriers

Armin Tahmasbi Rad,[†,§,⊥] Ching-Wen Chen,[∥,⊥] Wafa Aresh,[†,§,⊥] Yan Xia,[‡] Ping-Shan Lai,[*,∥] and Mu-Ping Nieh[*,†,‡,§]

[†]Department of Biomedical Engineering and [‡]Department of Chemical and Biomolecular Engineering, University of Connecticut, Storrs, Connecticut 06269, United States

[§]Polymer Program, Institute of Materials Sciences, University of Connecticut, 191 Auditorium Road, Storrs, Connecticut 06269, United States

[∥]Department of Chemistry, National Chung Hsing University, Taichung 402, Taiwan, ROC

Supporting Information

ABSTRACT: Combinatory modulation of the physical and biochemical characteristics of nanocarrier delivery systems is an emergent topic in the field of nanomedicine. Here, we studied the combined effects of incorporation of active targeting moieties into nanocarriers and their morphology affecting the enhanced permeation and retention effect for nanomedicine cancer therapy. Self-assembled lipid discoidal and vesicular nanoparticles with low-polydispersity sub-50 nm size range and identical chemical compositions were synthesized, characterized, and correlated with in vitro cancer cellular internalization, in vivo tumor accumulation and cancer treatments. The fact that folate-associated bicelle yields the best outcome is indicative of the preference for discoidal carriers over spherical carriers and the improved targeting efficacy due to the targeting ligand/receptor binding. The approach is successfully adopted to design the nanocarriers for photodynamic therapy, which yields a consistent trend in in vitro and in vivo efficacy: folate nanodiscs > folate vesicles > nonfolate nanodiscs > nonfolate vesicles. Folate discs not only have shown a higher tumor uptake and photothermal therapeutic efficiency, but also minimize skin photosensitivity side effects. The advantages of nanodiscoidal bicelles as nanocarriers, including well-defined size, robust formation, easy encapsulation of hydrophobic molecules (therapeutics and/or diagnostics), easy incorporation of targeting molecules, and low toxicity, enable the scalable manufacturing of a generalized in vivo multimodal delivery platform.

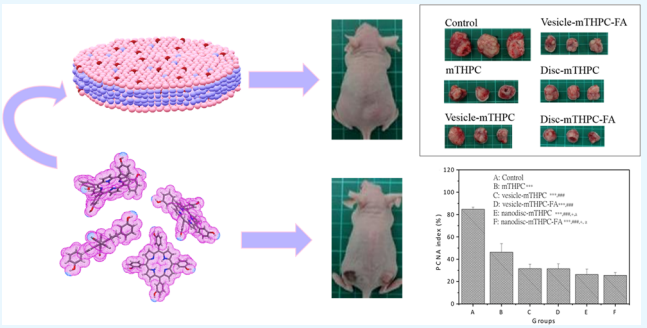

KEYWORDS: *EPR effect, nanodisc, in vivo animal model, small-angle X-ray scattering, photodynamic therapy*

1. INTRODUCTION

Nanoparticles (NPs) have been widely applied to biodiagnostic and pharmaceutical carriers, which enhance the potency of different applications. To date, three different generations of NPs have been introduced for clinical applications. The first generation of NPs was designed based on biocompatibility, water solubility, size, and charge density to enhance cellular uptake and toxicity.[1] The second-generation NPs are equipped with two important features: stealth and active targeting. The third generation shifted the paradigm of design to new shapes, more complicated structures, and "intelligent" platforms that can release their payload on demand (by environment or external stimuli) and have the therapeutic/diagnostic (theranostic) property.[2]

In regard to cancer treatment or diagnosis, several important properties of NPs are desirable, such as high biocompatibility, long in vivo circulation half-life, high accumulation at cancer tissues, and high loading drug/diagnostic capacity. Significant attention has been drawn to a variety of nanocarriers, such as solid lipid NPs,[3] liposomes,[4] polymeric micelles,[5] dendrimers,[6] oil bodies,[7] aptamers,[8] and nanoporous lipid bilayers,[9] demonstrating great potential for in vivo applications. That is due to their large capacities as drugs carriers, passive accumulation in malignant and inflamed tissue areas, long circulation times, and adaptability to multiple functions.[5]

NPs tend to selectively accumulate at the tumor sites via extravasation through the endothelial cells from the leaky vasculature, known as the "enhanced permeability and retention" (EPR) effect.[10] Based on recent findings, the physicochemical properties of the NPs (e.g., size, shape, charge, etc.) can be even more effective in tumor accumulation than simply using active targeting on the surface of nanoparticles.[11] Therefore, even in the absence of targeting ligands, nanomedicines can be designed to target a specific tissue better or be

Received: December 13, 2018
Accepted: February 22, 2019
Published: February 22, 2019

DOI: 10.1021/acsami.8b21609
ACS Appl. Mater. Interfaces 2019, 11, 10505−10519

nonspecifically absorbed by cells, by optimizing their physicochemical properties.[11] Recently, it has been proven that shape can also play a crucial role in cellular uptake.[12,13] There are multiple studies regarding morphology-dependent efficacy based on the same materials.[1,14] For instance, recent articles have shown an enhanced cellular uptake of self-assembled micelles compared to the vesicles synthesized with the exact same chemical composition.[15] However, the study on the efficacy of NPs with discoidal shape with sizes <50 nm remains limited.[16,17] Furthermore, a self-assembled platform with a controllable disc-to-vesicle transformation is unprecedented. The efficiency strongly depends on the physicochemical characteristics of the NPs, including both size and shape. It has been established that spherical NPs with a diameter range of 20−100 nm result in optimal tumor accumulation because of the EPR effect.[18] Nonetheless, different EPR effects have been reported to nonspherical nanostructures (i.e., nanorods). Nonetheless, different EPR effects have been reported for nonspherical nanostructures (i.e., nanorods) presumably due to their differences in vivo hydrodynamic behaviors, e.g., in vivo transport, circulation, and extravasation into the tumor.[19] For NPs larger than 100 nm, needle-like rods have exhibited the highest cellular uptake, followed by spheres, cylinders, and cubes as reported.[12,20] In the case of sub-100 nm NPs, spheres show some advantages over rods.[1] Here, we focused on comparing the efficacies of sub-100 nm discoidal NPs and optimized spherical carriers with a size of ∼50 nm.

Another commonly overlooked, but the important aspect is the scalability of the NPs. Recently, low-polydispersity, spontaneously forming discoidal bicelles have been found to be capable of entrapping hydrophobic molecules and having a robust formation/assembly mechanism. These bicelles are around 30 nm in diameter and 5 nm in thickness, and composed of short- and long-chain lipid molecules.[21] Nanodiscs are stable and soluble membrane mimetics. Their structure allows further modification such as affinity tags to the scaffold proteins. Thus, they can represent an appealing model system for isolation, solubilization, purification, and biophysical and biochemical studies of membrane proteins.[22,23] The platform allows large-scale nanomanufacturing of the NPs. A disc-to-vesicle structural transition also takes place as the long-chain lipid undergoes the change from the low-temperature gel (order) to the high-temperature L_α (liquid disorder) phase. Both nanodiscs and nanovesicles exhibit uniform dimensions. At low lipid concentrations, the nanovesicles irreversibly form and do not revert to nanodiscs even when the long-chain lipid becomes gel phase at a lower temperature.[21,24,25] These properties allow us to produce different low-polydispersity morphologies from a mixture of identical chemical compositions.[21]

However, the lack of specificity with passive targeting driven by the nanosize of NPs has limited efficacy. It has been suggested that active targeting to the tumors may enhance the intracellular uptake and minimize the NPs' distribution in healthy tissues. A reasonable strategy to achieve this goal is to utilize specific interactions between the overexpressed receptors of the cancer cells and the targeting molecules on the NPs' surface. Some ligands, such as folate and transferrin, can substantially increase site-specific targeting.[26] Particularly, folate has arisen as one of the targeting ligands for selective delivery of attached therapeutic and diagnostic agents due to the overexpressed folate receptor (FR) in a wide range of tumor tissues, such as lung, cervical, ovarian, kidney, breast, epithelial, colon, and brain tumors,[27] while limited in healthy tissues and organs. Folic acid is nonimmunogenic and stable over broad ranges of temperatures and pH values and can bind to the folate receptor after conjugation with drugs or imaging markers. Therefore, folic acid has been widely using used in cancer targeting therapy research works.[28] The application of folic acid has the advantages of its simplicity of conjugation to different NPs, its high binding affinity to FR ($K_d \sim 10^{-9}$ M),[29] and the extensive distribution of FR in a significant portion of human cancers.[30]

It is further reported that the fluidity of lipid membranes can vary with charge (negative or positive) and may induce local gelation.[31] Blood half-life is found the longest with neutral and slightly negative NPs.[32] NPs with positive charge are cleared relatively fast from the blood, resulting in the challenges of hemolysis and platelet aggregation.[12] The capability of our platform to fine-tune surface charge is another advantage besides size and shape control. In this study, the surface charge of the NPs is slightly negative for all of the samples.

Recently, photodynamic therapy (PDT) has been reported as a possible platform for cancer treatment. Using a light-induced chemical reaction, PDT agents can be activated to produce reactive oxygen species, damaging cancer cells. PDT is currently used in cancer therapy; however, its application is primarily limited due to the side effect on skin photosensitivity.[33,34] Moreover, most of PDT agents are hydrophobic and tend to aggregate, resulting in less production of $^1O_2$.[33] Here, we encapsulated *meta*-tetra(hydroxyphenyl) chlorin (*m*-THPC, Foscan), a clinically approved PDT agent for human use in Europe,[35] in both liposomes and nanodiscs and compared their efficacies for tumor reduction. Moreover, the impacts of folate as a targeting molecule on the enhancement of the cancer cellular uptake of both discoidal and vascular lipid-based self-assembly NPs were also evaluated. The sizes of both nanostructures were confirmed via dynamic light scattering (DLS) and small-angle X-ray scattering (SAXS). Fluorescence-activated cell sorting (FACS) and fluorescence confocal optical microscopy were used to quantify and visualize the cellular uptake of folate-conjugated NPs, respectively. A comprehensive structure−function relationship is studied to provide an insight into the choice of lipid-based NPs.

2. EXPERIMENTAL SECTION

2.1. Materials. Dipalmitoyl phosphatidylcholine (di-16:0, DPPC), dipalmitoyl phosphatidylglycerol (DPPG), dihexanoyl phosphatidylcholine (di-6:0, DHPC), poly(ethylene glycol) (PEG2000)-conjugated distearoyl phosphoethanolamine (DSPE-PEG2000), and folate poly(ethylene glycol)-conjugated distearoyl phosphoethanolamine (DSPE-PEG2000 Folate) were purchased from Avanti Polar Lipids (Alabaster, AL) and used without further purification. Nile Red (NR) and phosphate-buffered saline (PBS) powder were purchased from Sigma-Aldrich (St. Louis, MO). Sepharose CL-6B was purchased from GE Healthcare (Pittsburgh, PA). CellTiter-Blue kit was purchased from Promega (Madison, WI). Folate-deficient RPMI FD-RPMI medium, Dulbecco's phosphate-buffered saline (DPBS), and Hoechst 33342 were purchased from Life Technologies (Grand Island, NY). *meta*-Tetra(hydroxyphenyl)chlorin (*m*-THPC) was purchased from Cayman Chemical (Ann Arbor, MI).

2.2. Synthesis of Folate-Conjugated Lipid NPs of Different Shapes. (DPPC), (DPPG), (DHPC), (DSPE-PEG2000), (DSPE-PEG2000 Folate), and (NR) were used for NPs preparation. The molar composition of the mixture DPPC/DHPC/DPPG/DSPE-PEG2000/DSPE-PEG2000-Folate/NR is prepared at a ratio of 66.58/25.1/3.76/4.5/0.5/0.002.[23] All components of the required weights were first homogenized in chloroform. After the removal of the solvent by a vacuum oven, the dried samples were then redispersed in filtered deionized water to make stock suspensions with a total lipid weight

DOI: 10.1021/acsami.8b21609
ACS Appl. Mater. Interfaces 2019, 11, 10505−10519

concentration, C_{lp} of 10 wt %. After successive vortex and temperature cycling between 25 and 70 °C, the stock dispersions were then progressively diluted at room temperature to C_{lp} = 1.0 mg/mL with phosphate-buffered saline (PBS) solution. Vesicles were formed by increasing the temperature of 1.0 mg/mL discs solution to 55 °C for several hours.[10]

The *m*-THPC-entrapped bicelles were prepared at an *m*-THPC/lipid molar ratio of 1:200 homogeneously dispersed in chloroform. After being dried, the sample was rehydrated in water to form 10 wt % mother solution. After temperature cycling, the solution was centrifuged at 5000 rpm for 5 min in a Beckman Coulter centrifuge to separate the aggregates and large particles out. Further dilution to the desired concentration was performed prior to the use for in vivo study.

2.3. Nanoparticles Characterization. *2.3.1. Small-Angle X-ray Scattering (SAXS).* All of the samples were prepared at a concentration of 10 mg/mL in deionized water. Before SAXS measurements, the samples were put in an ultrasonic bath for 30 min and vortexed for 10 min. For each measurement, 70 μL of the solution was loaded in a standard quartz capillary (designed by Bruker) of 1.5 mm path length. The background (empty cell) and transmission of each sample were collected before each experiment. SAXS measurements were conducted using the Bruker Nano-STAR instrument, which has a Turbo X-ray source with rotating anode to generate the X-ray. By using a Göbel mirror, the wavelength (λ) of 1.542 Å produced by Cu K_α was employed. Two "scatterless" pinholes with the size of 500 and 350 μm, respectively, were used to collimate the beam. Data were collected by a MikroGap VÅNTEC-2000 detector. The sample-to-detector distance was set at 108 cm, which covers a q range ($q \equiv \frac{4\pi}{\lambda} \sin \frac{\theta}{2}$, where θ is the scattering angle) of 0.009−0.25 Å^{-1}. SAXS intensity is expressed as a function of q. Circular average and q-conversion of data were performed using the software provided by Bruker.

2.3.2. Dynamic Light Scattering (DLS). Size and population distribution of folate and nonfolate nanodiscs and vesicles were determined by ALV/CGS-8F/4 (ALV compact goniometer system, Germany) instrument equipped with a 632.8 nm laser beam. Both folate conjugate bicellar nanodiscs and nanovesicles were characterized. The samples were dissolved in ultrapure distilled filtered water to 0.1 wt % and vortexed before each measurement. The results were the average of 10 times measurements.

2.3.3. Negative-Staining Transmission Electron Microscopy (ns-TEM). The ns-TEM images of the samples were taken using FEI Tecnai T12. TEM samples were prepared by a drop (5 μL) of 0.001 wt % aqueous solution on a 400 mesh Formvar/carbon film copper grid (Electron Microscopy Sciences, PA). Negative staining was then applied with 10 mg/mL uranyl acetate (SPI Supplies, PA). Afterward, the extra sample was removed and the grids were dried at 25 °C. TEM was performed at 80 kV.

2.3.4. Calculation of Molecular Lipophilic Surface Potential (MLSP). MLSP describes the combined lipophilic influence of all fragments of a molecule[36] and can be calculated at given points in space.[37] MLSP analysis of *m*-THPC molecule was carried out using the Molinspiration Property Calculation Service molecular modeling package to study the feasibility of their encapsulation inside the lipid bilayers of nanodiscs and liposomes.[38] The surfaces were generated by assigning the Gasteiger −Hückel charges to the TMS structure atoms. The color scale for the MLSP includes a range from violet/blue, which represents higher lipophilicity, to red, for lower lipophilicity.

2.4. In Vitro Studies. FR-overexpressing human cervix carcinoma KB cells were maintained in FD-RPMI medium supplemented with 10% heat-inactivated fetal bovine serum at 37 °C in a 5% CO_2 and 95% air-humidified atmosphere.

2.4.1. Viability and Cytotoxicity Assay. Cytotoxicity against KB cells of folate nanoparticles (discs and vesicles) was assessed by microculture tetrazolium (MTT) assay and compared with nonfolate NPs (discs and vesicles). Briefly, KB cells were cultured in 96-well plates at a density of around 5×10^3 cells/well. The cells were allowed to adhere overnight. A series of doses (range from 0 mg/mL as a control to 1.6 mg/mL) of folate or nonfolate nanoparticles were added to the cells in FD-RPMI medium at 37 °C. After incubation with cells for 24 h, 25 μL of MTT indicator dye was added to each well and the cells were incubated for another 4 h at 37 °C in the dark. The absorbance was measured at 570 nm using a microplate reader. The values were normalized to the control value (untreated cells) to obtain the percentage of cell viability.

2.4.2. Evaluation of the Effect of Folate Targeting on the Cellular Uptake. KB cells were plated in six-well plates at a density of 50×10^3 cells/well and allowed to adhere for 24 h prior to the assay. For analyses of NPs uptake, 20 μL of 1 mg/mL folate nanodiscs, folate nanovesicles, nonfolate nanodiscs (control), and none folate nanovesicles (control) were added to each well and incubation was carried out for 2 h at 37 °C. The cells were then washed twice with DPBS to remove unbound ligand. Afterward, they were removed from the wells by trypsinization, centrifuged, and resuspended in cold (4 °C) DPBS to block further FR trafficking. The uptake of NR-loaded NPs was quantitated by a Becton Dickinson FACSCalibur flow cytometer. A total of 10 000 cells were counted for each run, and data were collected for three samples from each treatment condition. CellQuest software was used for data analysis.

2.4.3. Confocal Microscopy for Uptake Visualization. The visualization of the folate NPs internalization to KB cells was done by a Nikon A1R confocal microscope using a 60 × oil immersion lens. Image acquisition was performed by Nikon Elements Ar software. The preimaging incubation procedure followed the same conditions for the FACS quantification except that cells were not removed from the well by trypsin. The laser beam intensity and the sensitivity of photodetector were kept constant for comparison of the relative fluorescence intensities between the different samples.

2.4.4. Mechanism of Uptake. FA receptors in KB cells were blocked by adding folic acid to verify that the uptake mechanism of folate-conjugated NPs is following the FR-mediated endocytosis. Briefly, 1 mM folic acid was added to each well after plating 50 000 cells/well in six-well plates. The cells were incubated for 30 min at 37 °C. Then, both folate and nonfolate NPs (discs and vesicles) were added to each well. After an additional 2 h of incubation, the cells were washed twice with DPBS and removed from the plate by trypsin, centrifuged, and resuspended in cold (4 °C) DPBS to block further FR trafficking. The quantification was performed using FACS and confocal microscopy.

2.4.5. Intracellular Localization Study. To follow intracellular trafficking of nanoparticles, 1×10^5 KB cells were seeded on 15 mm glass coverslips and incubated at 37 °C for 24 h. Then, folate or nonfolate NPs (discs and vesicles; lipid concentration: 0.1%) were added to cells and incubated for 6 h. Following the incubation, the cells were treated with LysoTracker Green DND-26 (the guideline was provided by Invitrogen) for 30 min, followed by washing three times with HBSS buffer and fixing with 4% paraformaldehyde at room temperature. The coverslips were mounted onto a glass slide. Then, the colocalization of nanoparticles within LysoTracker-labeled cellular compartments was examined by confocal laser scanning microscopy (CLSM; Leica-SP5, Leica Microsystems Heidelberg GmbH, Germany). The colocalization ratio of nanoparticles within LysoTracker was quantified by MetaMorph software (Molecular Devices). All images were converted into 24 bits. The images of the two channels were automatically thresholded. MetaMorph "Measure colocalization" tool was used to determine the area pixel value of Nile Red and the area pixel value of LysoTracker. The percentage of overlapping was calculated by the following formula

$$\text{overlapping percentage} = \frac{\text{Nile Red area}}{(\text{Nile Red area} + \text{lysotracker area}) - \text{overlapping area}} \times 100\% \quad (1)$$

2.5. Tumor Penetration and Accumulation of Folate Lipid NPs in Vivo. The noninvasive animal study using an in vivo imaging system (IVIS) was approved by the Institutional Animal Care and Use Committee of the National Chung Hsing University. Female athymic nu/nu (nude) mice (age: 6−10 weeks) were purchased from LASCO, Taiwan. KB cells (1×10^7 per mouse) were sterilely inoculated subcutaneously in the right flank of nude mice. When the tumors reached a volume of around 500−1000 mm^3, 200 μL of folate or nonfolate NPs (discs and vesicles; lipid concentration: 2%) were

DOI: 10.1021/acsami.8b21609
ACS Appl. Mater. Interfaces 2019, 11, 10505−10519

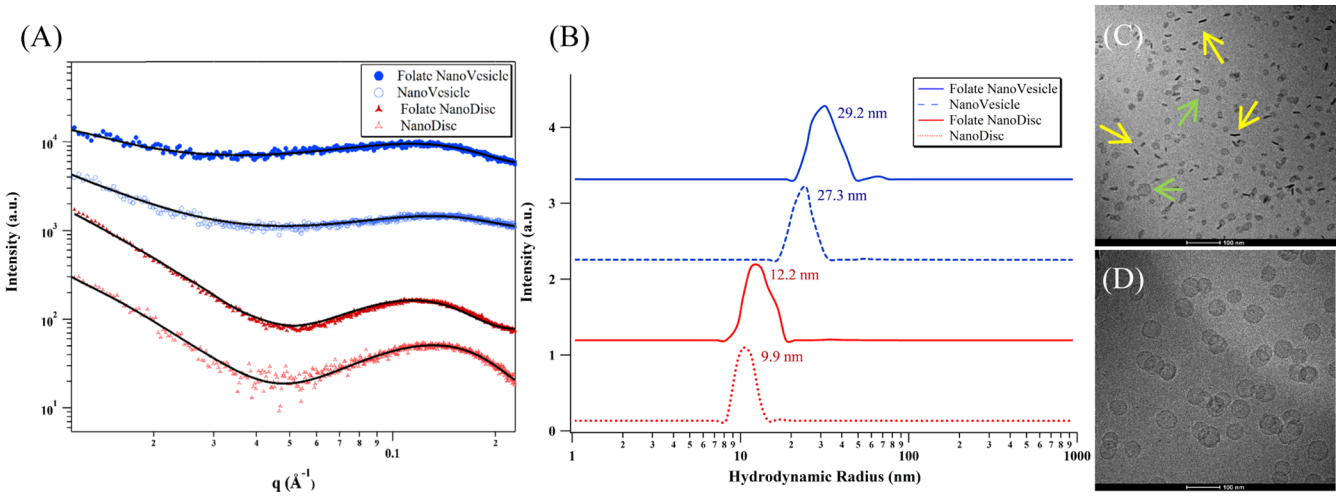

Figure 1. (A) SAXS characterization of nanodiscs and nanovesicles. The solid black lines show the best-fitting results for the scattering results. Related outcome data are shown in Table 1 based on these fittings. (B) Size distribution of nanodiscs and nanovesicles in the presence (solid line) and absence (dotted line) of folate ligand. The hydrodynamic radius, R_H, of NPs was 10−12 nm for nanodiscs and 27−30 nm for nanovesicles, consistent with the best-fitting dimensions from SAXS data. TEM images of the (C) bicelles and (D) liposomes show consistent outcome with the SAXS best-fitting results and hydrodynamic radii from DLS. The planar and edge-on views of the NDs are pointed by the green and yellow arrows, respectively.

injected via the tail vein intravenously (iv). The images were recorded via a Caliper IVIS system (excitation: 535 nm; emission: 600 nm) at different time points after injection. The fluorescence intensities were quantified for each sample by Living Image software.

2.6. In Vitro Studies of Photodynamic Activity of the NPs. *2.6.1. In Vitro Cytotoxicity of m-THPC-NPs.* Cellular cytotoxicities of free *m*-THPC, *m*-THPC-NPs, and *m*-THPC-FA-NPs were tested in vitro against KB cells by MTT cell viability assay. KB cells were cultured in a 96-well plate at a density of 1×10^4 cells/well. After incubation at 37 °C overnight, various concentrations of free *m*-THPC (BioLITEC PHARMA, Edinburgh, U.K.), nanodisc-*m*-THPC, nanodisc-*m*-THPC-FA, vesicle-*m*-THPC, and vesicle-*m*-THPC-FA were added to cell media in each well. After 24 h, the media were removed and the cells were washed with DPBS. KB cells were irradiated with a light dose (10 J/cm^2) of 660 nm laser. Next day, the MTT solution was added to each sample, followed by 4 h of incubation at 37 °C. The MTT solution was then replaced by 100 μL of dimethyl sulfoxide in each well. Using a scanning multiwell plate reader (SpectraMax M2^e, Molecular Devices, Sunnyvale), the cell viabilities were measured at 570 nm. The cell viability was calculated by the following equation: cell viability (%) = $Abs_{sample}/Abs_{control} \times 100\%$. Here, Abs_{sample} represents the absorbance of the cells incubated with free *m*-THPC, nanodisc-*m*-THPC, nanodisc-*m*-THPC-FA, vesicle-*m*-THPC, and vesicle-*m*-THPC-FA, and $Abs_{control}$ is the absorbance of untreated cells (positive control).

2.6.2. Flow Cytometry Studies of m-THPC-NPs. Cellular binding/uptake was measured by a flow cytometer. KB cells were cultured in a 6 cm culture dish at a density of 1×10^6 in folate-free RPMI 1640 medium for 24 h. The cells were pretreated with or without 1 mM folic acid for 30 min. After washed with 1xPBS, the KB cells were exposed for 1 h at 37 °C to nanodisc-*m*-THPC, nanodisc-*m*-THPC-FA, vesicle-*m*-THPC, and vesicle-*m*-THPC-FA, whose concentrations were fixed at 0.1 μg/mL of *m*-THPC during the experiment. The KB cells were trypsinized and resuspended in PBS. The samples were then quantitatively measured by an Accuri C6 flow cytometer (BD Accuri Cytometers, Ann Arbor, MI). The uptake and intracellular accumulation of *m*-THPC-NPs and *m*-THPC-FA in the KB cells were evaluated by flow cytometry. A total of 1×10^6 cells were incubated in the 6 cm culture dish for 24 h and then were treated with nanodisc-*m*-THPC, nanodisc-*m*-THPC-FA, vesicle-*m*-THPC, and vesicle-*m*-THPC-FA in a medium containing 0.1 μg/mL *m*-THPC for 2 or 24 h. After removing the medium, the cells were washed two times with DPBS. Then, the cells were trypsinized and resuspended in DPBS. The fluorescence intensity of the samples was then quantitatively measured by the Accuri C6 flow cytometer at a 488 nm excitation and with a 670 nm long pass filter. The Accuri C6 (version 1.0.264.21) was utilized to quantify the cellular uptake.

2.6.3. Intracellular Localization Study of NP-m-THPCs. To follow intracellular trafficking of free *m*-THPC, NP-*m*-THPCs, and NP-*m*-THPC-FAs, 1×10^5 KB cells were seeded on 15 mm glass coverslips and incubated at 37 °C for 24 h. Then, nanodisc-*m*-THPC, nanodisc-*m*-THPC-FA, vesicle-*m*-THPC, and vesicle-*m*-THPC-FA (*m*-THPC concentration: 0.1 μl/mL) were supplemented into cells and incubated for 2 h. After incubation, the cells were treated with LysoTracker Green DND-26 (the guideline was provided by Invitrogen) for 30 min, followed by washing three times with HBSS buffer and fixing with 4% paraformaldehyde at 25 °C. The coverslips were mounted onto a glass slide. Then, the colocalization of nanoparticles within LysoTracker-labeled cellular compartments was examined by CLSM. The colocalization ratio of nanoparticles within LysoTracker was quantified by MetaMorph software.

2.7. In Vivo Studies of Photodynamic Activity of the NPs. *2.7.1. Antitumor Activity of NP-m-THPCs in Vivo.* Female athymic nu/nu (nude) mice (5 weeks old, 20 ± 2 g) were purchased from LASCO, Taiwan, and antitumor studies were approved by the Institutional Animal Care and Use Committee of the National Chung Hsing University. All of the mice were kept in air-conditioned facility with artificial light−dark cycles and were provided standard food and filtered water. The tumor size was calculated as $\frac{1}{2}\left(\frac{4\pi}{3}\right)\left(\frac{L}{2}\right)\left(\frac{W}{2}\right)H$, where *L*, *W*, and *H* are the length, width, and height of the tumor, respectively. The treatments started when the tumor size reached a volume of approximately 100 mm^3 (as "day zero"). The mice were randomized into six treatment groups (n = 3 per group). PBS (control), free *m*-THPC, vesicle-*m*-THPC, vesicle-*m*-THPC-FA, nanodisc-*m*-THPC, or nanodisc-*m*-THPC-FA was used at a concentration of 0.3 mg/kg for tail vein injection. After 24 h, the tumor was irradiated by a diode laser at 661 nm with 15 J/cm^2 and tumor size and body weight of the mice were measured every 3 or 4 days. The skin photosensitivity was evaluated in mice treated with free *m*-THPC, vesicle-*m*-THPC, or nanodisc-*m*-THPC without or with FA conjugation. The degree of normal skin damage after PDT treatment was evaluated using a quantitative skin scoring system.[39]

2.7.2. Histological and Immunohistochemical Analysis. For histological examination, the tumor samples fixed in formalin (10%), dehydrated, and embedded in paraffin and tumor sections were stained with hematoxylin and eosin (H&E) and proliferating cell nuclear antigen (PCNA). The sections were deparaffinized in xylene followed by rehydration, incubated in 3% H_2O_2 to inhibit endogenous peroxidase activity, blocked with 5% skim milk, and then incubated

DOI: 10.1021/acsami.8b21609
ACS Appl. Mater. Interfaces 2019, 11, 10505−10519

Table 1. Best-Fitting Parameters Obtained from the SAXS Data of the NPs

	core−shell discoidal model (with invariant $t_{s,norm}$ = 14.9 Å, $\rho_w = 9.40 \times 10^{-6}$ Å^{-2} and $\rho_{s,norm} = 1.06 \times 10^{-5}$ Å^{-2})				
	ρ_{rim} ($\times 10^{-6}$ Å^{-2})	t_{rim} (Å)	ρ_{disc} ($\times 10^{-6}$ Å^{-2})	t_{disc} (Å)	R_{disc} (Å)
nanodisc	9.8 (±0.1)	23.5 (±0.5)	8.5 (±0.1)	26.6 (±0.2)	101 (±8)
folate nanodisc	9.8 (±0.1)	23.9 (±0.6)	8.7 (±0.2)	28.9 (±0.3)	115 (±11)

	core−three-shell spherical model (with invariant $\rho_w = \rho_{core} = 9.40 \times 10^{-6}$ Å^{-2})						
	ρ_{shells} ($\times 10^{-6}$ Å^{-2})			t_{shell} (Å)			
	shell 1	shell 2	shell 3	shell 1	shell 2	shell 3	R_{core} (Å)
nanovesicle	10.3 (±0.9)	9.0 (±0.1)	10.0 (±0.7)	6.8 (±4.1)	26.3 (±0.8)	12.4 (±4.5)	232 (±45)
folate nanovesicle	10.1 (±0.9)	8.9 (±0.1)	10.1 (±0.6)	8.2 (±4.5)	25.3 (±0.8)	12.9 (±4.6)	239 (±49)

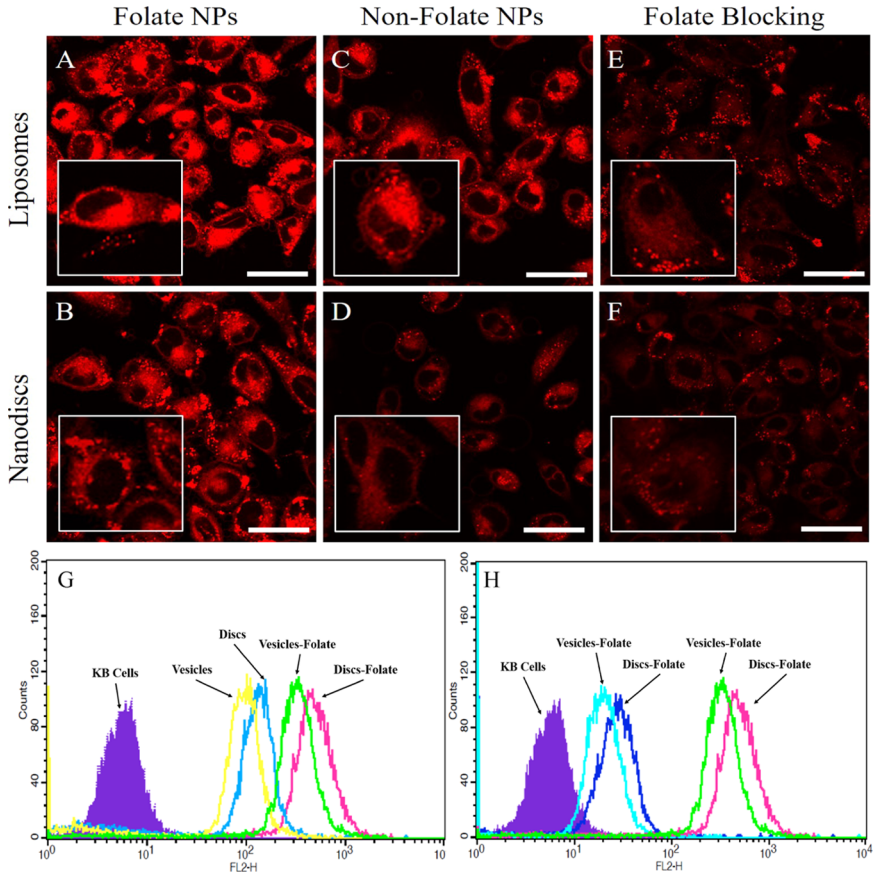

Figure 2. (A−F) Confocal micrographs representing the uptake of folate NPs: (A) folate discs, (B) folate vesicles, (C) nonfolate discs, (D) nonfolate vesicles, and (E, F) folate discs and folate vesicles after the addition of free folate into culture media. The scale bar is 20 μm. (G) FACS data of the cellular uptake of folate and nonfolate NPs by the KB cells after 2 h of incubation at 37 °C. The result shows that the uptake level follows: folate discs > folate vesicles > discs > vesicles. (H) FACS analysis of folate-mediated endocytosis. The uptake of folate NPs was reduced after the addition of free folate. The dark blue line shows reduction in the case of folate discs compared to the pink line, and the light blue line indicates reduction in the case of folate vesicles compared to the green line.

with primary PCNA antibodies (PC10, 1:200, Dako, Denmark). The sections were then incubated with the biotinylated secondary antibody for 30 min, and 3,3′-diaminobenzidine tetrahydrochloride chromogen was used to visualize avidin−biotin complexes. The stained sections were observed at low power (40×) and counted at high-power magnifications (400×). The cancer cells in the slides of each tumor were counted in 10 randomly selected microscope fields at 400× magnification using an Olympus BX 50 microscope. The percentage of PCNA-stained cells was analyzed using AlphaEaseFC (Alpha Innotech).

2.8. Statistical Analysis. Standard deviation (SD) is included in the expression of the experimental data in the form of (mean ± SD) for both in vitro and in vivo studies. The tumor volumes are monitored and recorded as a function of time. A linear mixed model with Bonferroni correction is applied to examine the group effects on tumor. The data were presented as the estimated marginal means (EM means) with the corresponding 95% confidence interval of tumor volume. The time effects were also considered. SPSS 11.0 software package (SPSS Inc., Chicago, IL) was used for statistics analyses, and statistical significance was set at 0.05.

3. RESULTS

3.1. NP Structural Characterization. SAXS is a characterization method which allows for morphological identification through simulating the electron density distribution of proposed NP structures. Figure 1A shows the SAXS data of 1.0 wt % of folate nanodisc, folate nanovesicle, nanodisc, and nanovesicle. The general scattering feature contains a broad peak between q = 0.07 and 0.20 Å^{-1}. Bilayer has a lipophilic core (hydrocarbon

DOI: 10.1021/acsami.8b21609
ACS Appl. Mater. Interfaces 2019, 11, 10505−10519

chains) being sandwiched by two shells of hydrophilic phosphatidylcholine headgroups, which have the highest electron density in the system (greater than those of hydrocarbon tails and water). Therefore, the electron density profile across the bilayer (i.e., water−headgroup shell−hydrocarbon core−headgroup shell−water) can be approximated as a "square well". Hence, the broad peaks in the SAXS results are corresponding to the correlation length of headgroup-to-headgroup distance.

To further interpret the SAXS data, we used a core−shell (i.e., hydrocarbon core−phosphate shell) discoidal model to describe the bicellar nanodisc (Supporting Information) as reported in our other recent research papers.[22,23,40] The model is described by the following independent parameters: shell thicknesses (including radial and facial shell thicknesses, t_{rim} and $t_{s,norm}$, respectively), discoidal core thickness (t_{disc}), discoidal core radius (R_{disc}), electron densities of solvent (ρ_w), radial and facial shells (ρ_{rim} and $\rho_{s,norm}$, respectively), and discoidal hydrocarbon core (ρ_{disc}). For nanovesicles, a core−three-shell spherical model (Supporting Information) is applied for best fitting the SAXS data. This model assumes a water core with a radius of R_{core} and electron density ρ_{core} of ρ_w. The three shells represent two headgroup layers (high electron density due to phosphate-rich structure) sandwiching the hydrocarbon layer (low electron density). We define shells 1, 2, and 3 to be the headgroup of the inner leaflet, the hydrophobic layer regime, and the headgroup of the outer leaflet, respectively. The thickness and electron density of each shell are adjusted to best fit the SAXS data.

Most of the electron densities used in the two models can be found in the literature reported elsewhere.[2,40] Table 1 illustrates the best-fitting parameters for both models used for the four samples. The results indicate that the addition of folic acid has no effect on structural change but leads to a slight variation in dimensions.

The above-mentioned structures were confirmed by DLS and TEM results as shown in Figure 1B, which showed unimodal distributions of hydrodynamic radius (R_H) for nanodiscs (10−12 nm) and vesicles (27−30 nm). These dimensions were consistent with those obtained through the SAXS best-fitting result. The NPs containing folate ligand did exhibit a slightly larger R_H compared to those without folate. Both DLS and SAXS data indicated the absence of nanoparticle aggregation in the solution. The diameters of our vesicles (liposomes) are around 50 nm, which falls in the ideal size range for nanocarriers to utilize the targeting tumor.[12,41] Moreover, the ligand density is optimized.[41] Although enhanced EPR effect is also observed for 50−100 nm NPs, the cellular uptake is limited by the consumption of cell membrane receptors that bind to the targeting ligands of the NPs, reducing the total number of NPs that can be internalized by the cells. Mathematical modeling has also shown that optimal endocytosis should occur under the condition of no shortage of ligand on the NP or cell surface receptor.[41] On the other hand, nanoparticles smaller than 20 nm penetrate deep into the tumor extracellular matrix but may not retain beyond 24 h. It has also been shown that even addition of targeting moieties on the surface of the NPs does not affect tumor accumulation or biodistribution, and they are eliminated from the body through the renal system in a short period of time.[42]

3.2. Effect of Shape and Folate Targeting on the Cytotoxicity and Cellular Uptake. Figure S1 in the Supporting Information summarizes the outcomes of MTT assay where the cell proliferation counts were obtained after 24 h of incubation with KB cells. The results were compared to the control samples (untreated). No statistically significant toxicityfor the KB cells up to 1.6 mg/mL (the lipid concentration) was observed in all cases of NPs. The results indicate that all of the components making up the NPs are biocompatible.

Fluorescence confocal microscopy was conducted to investigate the cellular uptake of different NPs. The optical configuration was identical for all cases. Figure 2A−D shows the confocal micrographs of KB cells after being incubated with folate discs, discs, folate vesicles, and vesicles, respectively, for 2 h and rinsed twice in DPBS. The cellular uptake level of NPs shows a clear dependence of targeting folate and particulate morphology: folate discs > folate vesicles > pristine discs > pristine vesicles.

FACS was also used to evaluate the cellular uptake of NPs by KB cells. Figure 2G shows the FACS results of four different NPs (nonfolate discs, folate discs, nonfolate vesicles, and folate vesicles) under the same lipid concentration and Nile Red-to-lipid molar ratio. Each experiment was repeated at least three times. The outcome is consistent with the aforementioned confocal microscopy results, indicating the same sequence in the cellular uptake: folate discs > folate vesicles > discs > vesicles. The FACS and confocal microscopy images indicate that the uptake of folate discs is higher than that of folate vesicles by ca. 2−3-fold, consistent with our previous report on the morphological dependence of the cellular uptake of lipid-based self-assembled nonfolate NPs (i.e., nanodiscs and nanovesicles).[22] The addition of DSPE-PEG2000 folate on the surface of the NPs further enhances the KB cellular uptake by ∼7-fold. It has been reported that the uptake of monoclonal antibody-coated polystyrene nanoparticles in an experiment on the breast cancer cell line was found the highest in the case of rodlike NPs with length 367 nm and width 126 nm, followed by nanodiscs with diameter 236 nm and thickness 88 nm, the lowest for 200 nm spheres.[43] Our FACS results seem to suggest a similar trend even at a much smaller length scale (<50 nm), further confirming the roles of nanoscaled morphology and targeting molecules in the enhancement of cellular internalization. It is also noteworthy that the targeting effect, in this case, overwhelms the morphological effect since the folate vesicles show higher efficacy in cellular uptake than nonfolate discs do.

3.3. Mechanism of Enhanced Endocytosis by Folate Targeting. To confirm that the enhanced cellular uptake of folate-conjugated NPs originates from the overexpressed folate receptor-mediated endocytosis, we performed a similar FACS experiment under the same aforementioned condition except for free folate (at a concentration of 1.0 mM) being added in the cell growth medium.[44] Figure 2H shows the FACS results of the cellular uptake of folate lipid NPs by the KB cells. Compared to the outcome obtained from the medium in the absence of free folate, the cellular uptake was significantly reduced by an order of magnitude, supporting the proposed FR-regulated endocytosis. The higher level of cellular uptake of folate nanodiscs than that of folate vesicles remains valid even in the presence of free folate consistent, with our previous report revealing that nanodiscs effectively utilize two more endocytosis (namely, micropinocytosis and microtubule-mediated endocytosis) than the vesicles do, independent of the pathway through folate receptor.[22]

The FACS outcomes of the samples in the presence of excess free folic acid in the culture media are consistent with the

DOI: 10.1021/acsami.8b21609
ACS Appl. Mater. Interfaces 2019, 11, 10505−10519

micrographs of confocal fluorescence data (Figure 2E,F), indicating reduction of the uptake of folate NPs.

3.4. Tumor Penetration and Accumulation of Folate Lipid NPs in Vivo. For the initial observation of the in vivo EPR effect, we used Nile Red-labeled nanocarriers, which were administered by iv injection, and the fluorescence emission of the tumors was attributed to the accumulation of the nanoparticles in the tumor.

The tumor-targeting efficiencies of the folate and nonfolate NPs were assessed in vivo using KB tumor-bearing mice by the Caliper IVIS system. Folate nanodiscs exhibited a higher tumor uptake in comparison to folate vesicle at different time points. The same outcome regarding shape was also observed for nonfolate discs and nonfolate vesicles. The penetration rate and accumulation volume of NPs were folate disc > folate vesicle > nonfolate disc > nonfolate vesicle (Figure 3A, Tables 2 and 3).

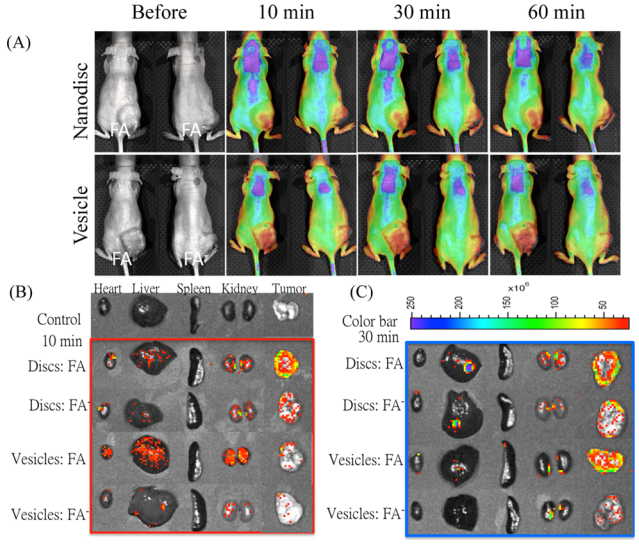

Figure 3. (A) In vivo fluorescence assessment of nanodiscs-Nile Red or vesicles-Nile Red with or without folate in nude mice bearing KB xenografts. The mice were intravenously administered with nanodiscs-Nile Red or vesicles-Nile Red with or without folate at 2% lipids, and the fluorescence signals were monitored at different time points. (B, C) Major organs of the mice after nanodiscs-Nile Red or vesicles-Nile Red with or without folate administration. The mice were sacrificed after intravenously administered with discs-Nile Red or vesicles-Nile Red with or without folate at 2% lipids, and the fluorescence signals were monitored at different time points. Section B is the result after 10 min and C is after 30 min.

The region of interest (ROI) tumor uptake analysis for different NPs has shown that addition of folate-targeting molecules increased the tumor uptake by factors of 26 and 43% on average for nanodiscs and vesicles in the first hour after injection, respectively. The nanodiscs, though having the same chemical composition as nanovesicles, are more effective in tumor uptake over a longer duration (25−46% increase). The major organs of the mice after nanodisc-Nile Red or vesicle-Nile Red with or without folate administration also showed the same results (Figure 3B,C, Tables 4 and 5). Note that the molar composition of the charged lipids, i.e., DSPE-PEG2000 and DPPG, remains constant for the different NPs. Therefore, the surface charge density should be identical and is not expected to give rise to the difference. It is reported that the circulation lifetimes of neutral and slightly negatively charged NPs are longer. Also, they accumulate less in the liver, spleen, kidneys, and lungs.[12,45] The tested NPs are in a similar range of such charge density. As such multilamellar or unilamellar vesicles have been used and proven to be efficacious in clinical drug delivery,[46] the nanodiscoidal bicelles seem to be an even better platform for this purpose.

Table 3. Fold Increasing of ROI in Tumor[a,b]

fold increasing of ROI					
Nanodisc: Nile Red	0 min	10 min	30 min	1 h	4 h
FA	1.00	6.27	5.89	4.70	1.88
FA⁻	1.00	4.88	4.66	3.80	1.99
Vesicle: Nile Red	0 min	10 min	30 min	1 h	4 h
FA	1.00	5.51	5.18	3.76	1.44
FA⁻	1.00	3.98	3.57	2.60	1.56

[a]The region of interest in the tumor was quantified by Living Image software. [b]FA and FA represent NPs in the presence and absence of folate, respectively.

In addition, the vasculature structures are different around the healthy tissues (tight) and cancerous tissues (with more defects). Therefore, the accessibility of NPs to folate receptor of healthy tissue is lower in comparison to the tumor.[47] Compared to Taxol, the lipid-shell and polymer-core nanoparticles and targeted delivery of paclitaxel modification with folate displayed better antitumor effect and lower toxicity in vivo. It is speculated that the folate-modified targeted delivery of paclitaxel nanoparticles resulted in more effective accumulation in tumor cells through ligand−receptor interactions for effective long-term therapeutic activity.[48] The folate-targeted vinca alkaloid conjugates-EC145 applied in KB tumor xenograft animal model also showed the excellent antitumor effect and did not observe toxicities in the organs.[49] For the above reasons, folate is one of the appropriate choices for targeting cancer. Here, the same strategy is therefore applied to *m*-THPC discs or *m*-THPC vesicles to examine the antitumor effect in KB tumor xenograft animal model in the following session.

3.5. Photodynamic Active Nanoparticles in Vitro Assessments. *3.5.1. PDT Efficacy of m-THPC-NPs in Human Oral Cavity Carcinoma Cells (KB, Contamination with HeLa Cells).* MLSP simulation of *m*-THPC molecules

Table 2. Quantification of ROI in Tumor by Living Image Software[a]

region of interest (ROI)					
Nanodisc: Nile Red	0 min	10 min	30 min	1 h	4 h
FA	5.30×10^{10}	3.32×10^{11}	3.13×10^{11}	2.49×10^{11}	9.97×10^{10}
FA⁻	1.32×10^{10}	6.42×10^{10}	6.12×10^{10}	5.00×10^{10}	2.61×10^{10}
Vesicle: Nile Red	0 min	10 min	30 min	1 h	4 h
FA	3.99×10^{10}	2.20×10^{11}	2.07×10^{11}	1.50×10^{11}	5.74×10^{10}
FA⁻	2.56×10^{10}	1.02×10^{11}	9.15×10^{11}	6.66×10^{10}	3.99×10^{10}

[a]FA and FA represent NPs in the presence and absence of folate, respectively.

DOI: 10.1021/acsami.8b21609
ACS Appl. Mater. Interfaces 2019, 11, 10505−10519

Table 4. Quantification of Region of Interest (ROI) in Organs by Living Image Software[a]

10 min	heart	liver	spleen	kidney	tumor
negative	8.71×10^8	1.74×10^8	4.15×10^8	7.49×10^8	1.52×10^8
Nanodisc: Nile Red					
FA	8.96×10^8	4.72×10^9	4.74×10^9	2.85×10^9	7.97×10^9
FA$^-$	7.67×10^8	3.09×10^9	5.97×10^9	2.56×10^9	3.66×10^9
Vesicle: Nile Red					
FA	1.13×10^9	7.34×10^9	6.36×10^8	3.80×10^9	2.79×10^9
FA$^-$	4.44×10^8	3.74×10^9	5.41×10^9	2.12×10^9	2.73×10^9
30 min	heart	liver	spleen	kidney	tumor
Nanodisc: Nile Red					
FA	4.62×10^8				
FA$^-$					
Vesicle: Nile Red					
FA	6.66×10^8	2.35×10^9	6.53×10^8	1.76×10^9	7.57×10^9
FA$^-$	3.93×10^8	1.60×10^9	3.74×10^8	2.21×10^9	2.97×10^7

[a]FA and FA represent NPs in the presence and absence of folate, respectively.

Table 5. Fold Increasing of ROI in the Tumor[a]

10 min	heart	liver	spleen	kidney	tumor
negative	1.00	1.00	1.00	1.00	1.00
Nanidisc: Nile Red					
FA	10.29	2.72	1.14	3.80	5.26
FA$^-$	8.81	1.78	1.44	3.42	2.41
Vesicle: Nile Red					
FA	12.97	4.23	1.53	5.07	1.84
FA$^-$	5.10	0.22	1.30	2.83	1.80
30 min	heart	liver	spleen	kidney	tumor
Nanidisc: Nile Red					
FA	5.31	4.69	1.10	4.11	5.73
FA$^-$	4.73	2.73	1.05	2.99	3.00
Vesicle: Nile Red					
FA	7.64	1.36	1.57	2.35	5.00
FA$^-$	4.52	0.92	0.90	2.95	1.96

[a]FA and FA represent NPs in the presence and absence of folate, respectively.

indicates a planar structure as well as high lipophilicity (Figure 4A), suitable for encapsulation in the bilayer. For phototoxicity measurement, the cells were irradiated with a laser (λ = 661 nm, power density = 15 J/cm^2) for 12 min and 30 s. Cell cytotoxicity was measured as the percentage of the viable cells over the untreated cell control. The results are shown in Figure 4B. The phototoxicities of free *m*-THPC were significantly higher than those of *m*-THPC NPs conjugated without or with FA at the same *m*-THPC dose, suggesting that free *m*-THPC is more effective in treating KB cells than *m*-THPC-NPs. With carriers, the phototoxicities of nanodisc-*m*-THPC-FA-treated cells showed that the cell viability significantly decreased over different dosages, much lower than other *m*-THPC-NP-treated cells. However, there was no difference between vesicle-*m*-THPC-FA- and nanodisc-*m*-THPC-treated groups.

3.5.2. Folate Receptor-Specific Cellular Binding and Uptake of m-THPC-Loaded NPs. To evaluate the role of folate in the cellular uptake of *m*-THPC-NPs, the cells were pretreated with free folic acid (10^{-3} M) for 30 min to inhibit folate-assisted uptake, followed by the addition of vesicle-*m*-THPC, vesicle-*m*-THPC-FA, nanodisc-*m*-THPC, or nanodisc-*m*-THPC-FA and incubated for another 1 h at 37 °C. Flow cytometry (Accuri C6 flow cytometer) was performed to detect the fluorescence of *m*-THPC in trypsinized KB cells. The cellular uptake of *m*-THPC decreased 79.9% in vesicle-*m*-THPC-FA groups due to the pretreatment of 10^{-3} M folate acid, while no effect was shown in vesicle-*m*-THPC groups (Figures 4G). For nanodiscs, the cellular uptake of *m*-THPC decreased by 56.9% in the nanodisc-*m*-THPC-FA group in the sample of pretreated folate acid compared to the nonpretreated one with no effect in the nanodisc-*m*-THPC group (Figure 4H). The result also shows that the uptake rate of nanodisc-*m*-THPC-FA is higher than that of vesicle-*m*-THPC-FA after folate pretreatment (nanodisc-*m*-THPC-FA: 41.8% and vesicle-*m*-THPC: 14%). The same trend in cellular uptake is found for non-folate acid-conjugated *m*-THPC NPs (vesicle-*m*-THPC: 0.2%, folate blocking-vesicle-*m*-THPC: 0.4%; nanodisc-*m*-THPC: 12.3%, folate blocking-nanodisc-*m*-THPC: 10.7%). This finding suggests that pretreatment of folate can effectively inhibit the uptake of nanodisc-*m*-THPC-FA and vesicle-*m*-THPC-FA, thus confirming the overexpression of folate for KB cells. As a result, nanodisc-*m*-THPC-FA and vesicle-*m*-THPC-FA were taken up by KB cells through the mechanism. However, the values of *m*-THPC uptake were no different in each group after 24 h incubation (Figure 4I). The histograms of fluorescence on KB cells incubated with either vesicle-*m*-THPC or nanodisc-*m*-THPC NPs with or without FA immobilization also show higher cellular uptake for discdoial NPs (Figure 4C–F). The fact that the cellular uptake and fluorescence intensity of folate-conjugated *m*-THPC NPs were higher than those of non-folate-conjugated *m*-THPC NPs in both groups of vesicles and nanodiscs suggests the enhanced efficacy of folate targeting. Moreover, the nanodiscs uniformly showed higher cellular uptake.

3.5.3. Intracellular Localization Study via Confocal Images of m-THPC-NPs in KB Cell. The intracellular localization of *m*-THPC-NPs was investigated with LysoTracker Green DND-26 (green). As shown in Figure 5, free *m*-THPC, nanodisc-*m*-THPC, or vesicle-*m*-THPC without FA conjugation were colocalized in lysosomes (free *m*-THPC: 89.76%; nanodisc-*m*-THPC: 86.48%; vesicle-*m*-THPC: 76.4%). It also shows that a strong fluorescence of folate-conjugated NPs was expressed in the cytoplasm. This indicates that cells internalized the NPs through endocytosis and distributed them in the cytoplasm after NPs escaped from the endosome and/or the lysosome (nanodisc-*m*-THPC-FA: 32.54%; vesicle-*m*-THPC-FA: 39.86%).

DOI: 10.1021/acsami.8b21609
ACS Appl. Mater. Interfaces 2019, 11, 10505–10519

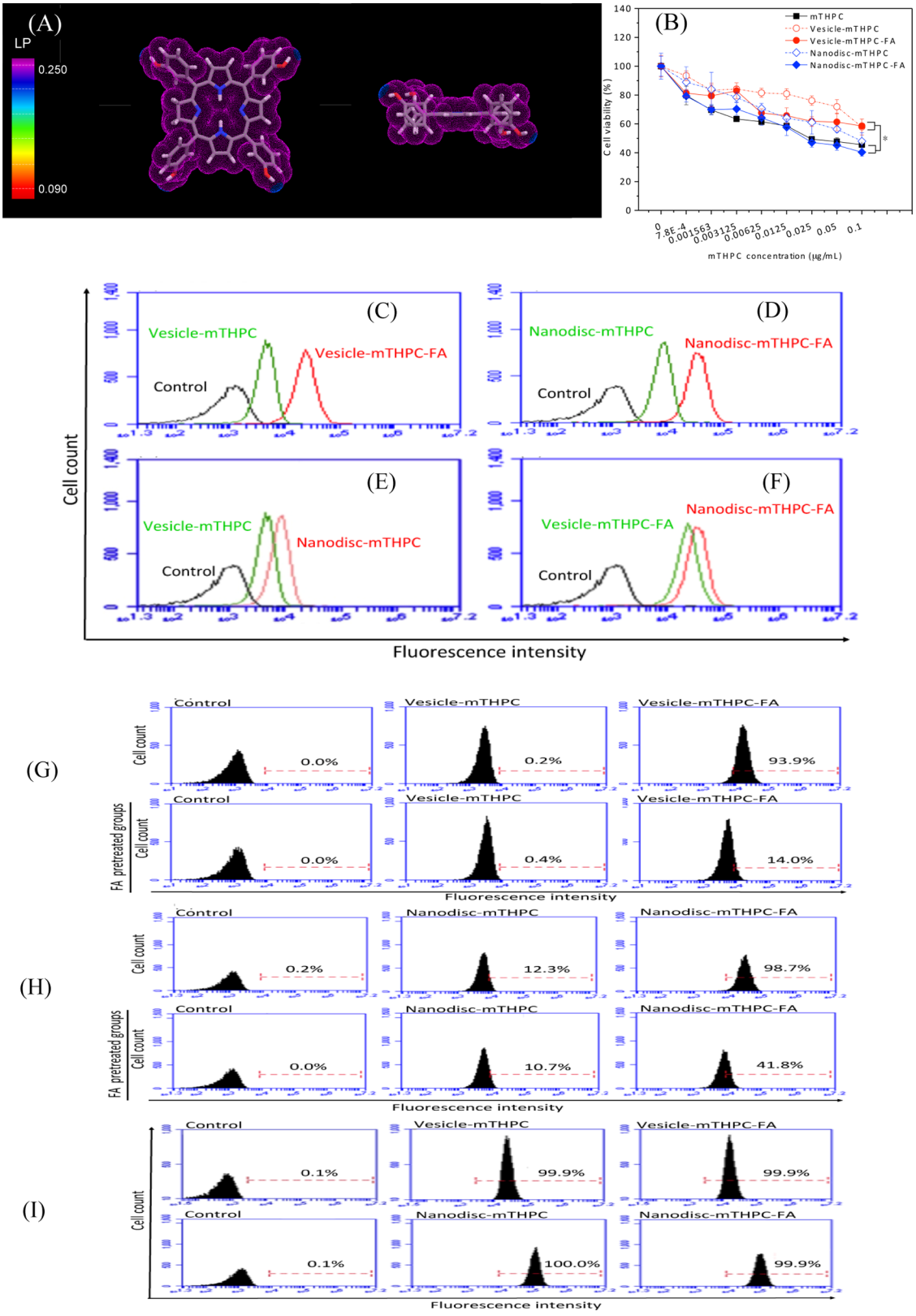

Figure 4. (A) MLSP analysis of *m*-THPC molecule showing its highly lipophilic structure. Result is shown in side and top views. (B) Cytotoxicities of human oral cavity carcinoma cells (KB) cells, when cells were incubated with free *m*-THPC, vesicle-*m*-THPC NPs, or nanodisc-*m*-THPC NPs conjugated without or with FA and irradiated with a 10 J/cm^2 light dose. (C−F) Flow cytometry histogram profile of KB cells: (C) vesicle-*m*-THPC and vesicle-*m*-THPC-FA, (D) nanodisc-*m*-THPC and nanodisc-*m*-THPC-FA, (E) vesicle-*m*-THPC and nanodisc-*m*-THPC, and (F) vesicle-*m*-THPC-FA and nanodisc-*m*-THPC-FA for 2 h at 37 °C. Cellular uptake incubated with vesicle-*m*-THPC NPs or nanodisc-*m*-THPC NPs conjugated without or with folate (*m*-THPC concentration 0.1 μg/mL) for (G−H) 1 h (with or without pretreatment of folic acid at 37 °C) and for (I) 24 h at 37 °C without pretreatment of folic acid.

DOI: 10.1021/acsami.8b21609
ACS Appl. Mater. Interfaces 2019, 11, 10505−10519

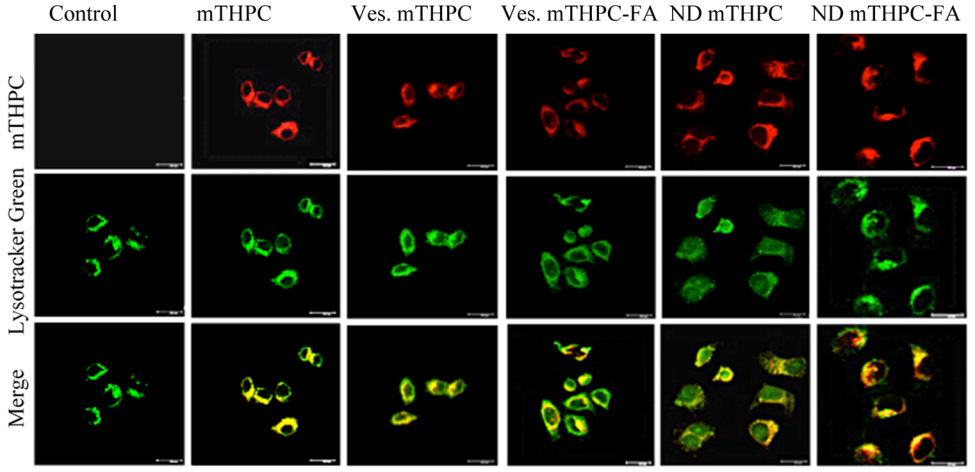

Figure 5. Fluorescent images were utilized to assess the colocalization of vesicle-*m*-THPC or nanodisc-*m*-THPC NPs conjugated with or without FA (red) with lysosomes using LysoTracker (green). The colocalization ratio of nanoparticles within LysoTracker was quantified by MetaMorph software. The scale bar is 10 μm.

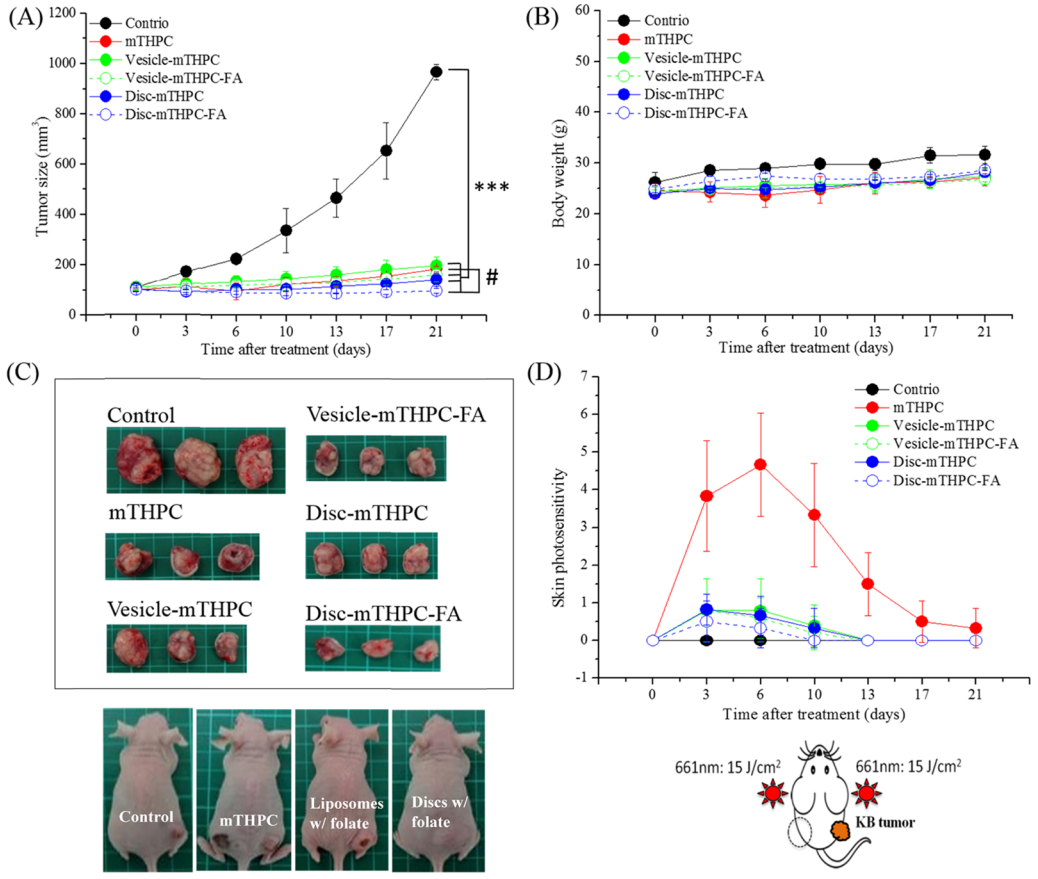

Figure 6. Antitumor effect of vesicle-*m*-THPC and nanodisc-*m*-THPC NPs in vivo. Experimental design of the photodynamic therapy is also shown. Tumor of KB cells were implanted to the right flank of the nude mice. (A) KB cells tumor development curve. The size of the tumors was measured every 72−96 h. (B) Relative weight curves of the animals. (C) Representative photos of tumors in each treatment group on day 21. Data are presented as mean ± standard deviation (SD). (Bottom) Images of the mice after 4 days of one-time treatment. A clear skin burning mark on the left flank was found in the case of free *m*-THPC, while the control mice (no treatment) and the mice treated by *m*-THPC-containing NPs before NIR exposure show no significant effect on the left frank. (c) Sizes of the tumors harvested from the mice after 21 days of treatment. (d) The volume of the tumors evolved as a function of time for each group. (D) Skin photosensitivity at various time points after PDT treatment. Data are presented as mean ± SD. (*) Significant difference compared to control ($p < 0.001$), (#) Significant difference compared with *m*-THPC; $n = 3$.

Mansoori and co-workers demonstrated that folate-conjugated NPs attached to the folate receptors, followed by uptake through a caveolae-mediated endocytotic pathway.[50] Cuong et al. showed that the folate-decorated star-shaped PEG−PCL micelle in MCF-7 was endocytosed via caveolae/lipid raft-mediated endocytosis and localized in the cytoplasm, not lysosome.[51] As shown in Figure 5, strong fluorescence spots of folate NPs were almost observed in the cytoplasm, indicating the

DOI: 10.1021/acsami.8b21609
ACS Appl. Mater. Interfaces 2019, 11, 10505−10519

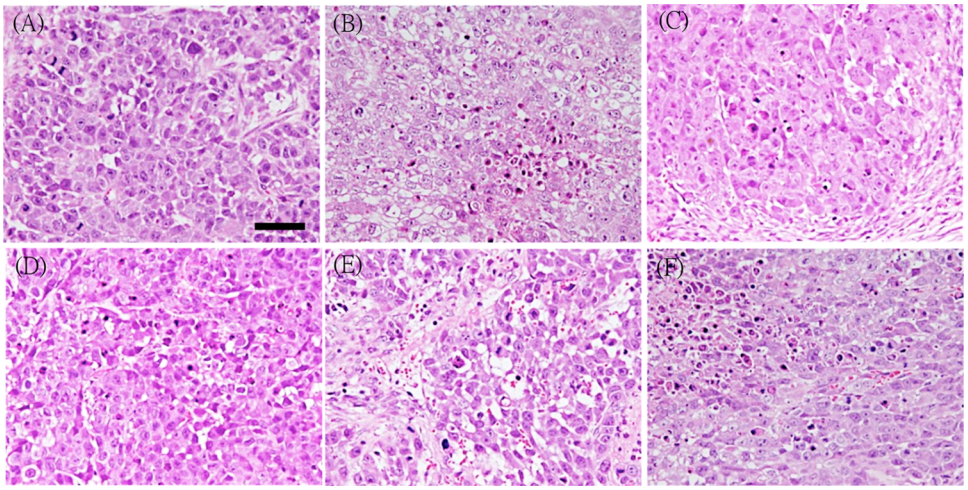

Figure 7. H&E staining of KB xenografted tumors treated with vesicle- or nanodisc-based *m*-THPC-mediated PDT without or with FA conjugation: (A) control, (B) free *m*-THPC, (C) vesicle-*m*-THPC, (D) vesicle-*m*-THPC-FA, (E) nanodisc-*m*-THPC, and (F) nanodisc-*m*-THPC-FA; $n = 3$. The scale bar is 50 μm.

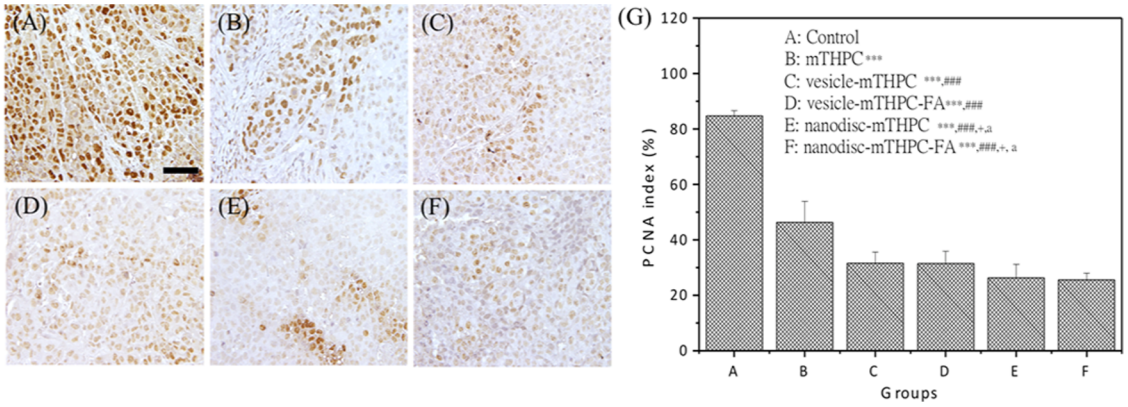

Figure 8. Immunohistochemical analysis of PCNA in KB xenograft tumors treated with vesicle- or nanodisc-based *m*-THPC-mediated PDT without or with FA conjugation: (A) control, (B) *m*-THPC, (C) vesicle-*m*-THPC, (D) vesicle-*m*-THPC-FA, (E) nanodisc-*m*-THPC, and (F) nanodisc-*m*-THPC-FA. (G) Cellular proliferation was analyzed by calculating the number of PCNA-positive cells with 400 magnification. (*) Significant difference compared with PBS control group ($p < 0.001$); (#) significant difference compared with *m*-THPC group ($p < 0.001$); (+) significant difference compared with vesicle-*m*-THPC group ($p < 0.05$); (a) significant difference compared with vesicle-*m*-THPC-FA group ($p < 0.05$); $n = 3$. The scale bar is 50 μm.

escape of internalized folate NPs from the endosome and/or the lysosome to the cytoplasm. Thus, folate discs can be endocytosed mainly via folate receptor and caveolin-mediated internalization pathways.

3.6. Photodynamic Therapy and Antitumor Effect of *m*-THPC NPs: in Vivo Study. To further investigate vesicle- and bicelle-based *m*-THPC-mediated PDT in vivo, we performed folate receptor-targeted or nontargeted PDT treatment via intravenous injection using the KB tumor model in nude mice. As shown in Figure 6A, tumor volumes continuously increased from day 0 to day 21 in the PBS control group. In the PDT groups (free *m*-THPC, vesicle-*m*-THPC, vesicle-*m*-THPC-FA, nanodisc-*m*-THPC, and nanodisc-*m*-THPC-FA), tumor volumes were significantly reduced compared to those of the control group ($p < 0.001$), indicating efficient *m*-THPC-mediated photochemical toxicity against cancer. Moreover, both vesicle-*m*-THPC-FA (TGI = 84.0%) and nanodisc-*m*-THPC-FA groups (TGI = 90.2%) suppressed the tumor growth compared to the *m*-THPC groups ($p < 0.05$), whereas no significant differences were observed among *m*-THPC, vesicle-*m*-THPC, and nanodisc-*m*-THPC groups, suggesting that FA conjugation improves tumor accumulation and cellular internalization of nanocarriers in the folate receptor-overexpressed KB xenografted tumor, resulting in efficient PDT efficacy against cancer. Compared to vesicle-*m*-THPC group (TGI = 80.1%), smaller tumor volumes were observed in vesicle-*m*-THPC-FA (TGI = 84.0%) and nanodisc-*m*-THPC (TGI = 85.8%) groups on day 21; however, no significant differences in tumor volume were found among these groups. It is noted that nanodisc-*m*-THPC-FA with irradiation revealed significantly improved PDT efficacy, more than 90.2% tumor growth inhibition compared to that of the *m*-THPC-mediated PDT group (TGI = 81.6%. $p < 0.05$) and the vesicle-*m*-THPC group (TGI = 80.1%. $p < 0.05$). No significant difference was observed between nanodisc-*m*-THPC-FA and nanodisc-*m*-THPC groups. The differences in body weight among the six groups were similar, and no obvious weight loss was observed (Figure 6B). Figure 6C illustrates the tumor photos of each group on day 21, and significantly smaller tumor sizes were observed in PDT groups compared to the control group. Skin photosensitivity of control and PDT-treated groups is shown in Figure 6D,E. Mice receiving free *m*-THPC revealed obvious photodamages on normal skin (left flank, day

DOI: 10.1021/acsami.8b21609
ACS Appl. Mater. Interfaces 2019, 11, 10505−10519

4) after irradiation, although *m*-THPC is the second generation of photosensitizers with less phototoxicity to the skin. Vesicle- and nanodisc-based *m*-THPC delivery system without or with FA conjugation significantly reduces skin photodamages of the original *m*-THPC formulation. These results clearly showed that the utilization of the nanodisc-*m*-THPC-FA reduced the drug accumulation in normal tissues, caused less skin photosensitivity, and improved the photothermal therapy efficacy through targeting delivery systems.

3.6.1. Effect of Free m-THPC and m-THPC NPs-Mediated PDT on Cellular Proliferation. To assess the antitumor activities with free *m*-THPC or *m*-THPC NPs-mediated PDT, the excised tumor tissues were fixed and prepared for H&E staining and PCNA staining. As shown in Figure 7, significant differences in tissue morphology between control and PDT treatment groups were observed in H&E-stained tumor sections. The control section showed that tumor cells had a compact, dense tissue structure and consisted of large polymorphic cells tightly packed together. The treated groups showed that prominent necrosis is clearly apparent in the free *m*-THPC (Figure 7B), vesicle-*m*-THPC (Figure 7C)-, vesicle-*m*-THPC-FA (Figure 7D)-, nanodisc-*m*-THPC (Figure 7E)-, and nanodisc-*m*-THPC-FA (Figure 7F)-mediated PDT groups. To investigate the cell proliferation status of the treated and control tumors, PCNA that was synthesized in the late G1 and S phases in the cell cycle acted as a proliferation staining agent. As shown in Figure 8, a high percentage index of PCNA expression (85.93 ± 2.63%) was observed in the control group (Figure 8A). In contrast, tumor from PDT-treated mice exhibited significantly decreased cell proliferation, as detected by PCNA expression (Figure 8B−F), compared to the control group ($^{*}p < 0.001$). Vesicle- or nanodisc-based *m*-THPC delivery system without or with FA conjugation presented a significantly lower rate of cell proliferation compared to *m*-THPC-mediated PDT group (45.95 ± 2.94%, $^{\#}p < 0.001$). FA-conjugated (25.59 ± 2.40%) or nonconjugated nanodisc-based *m*-THPC (26.28 ± 4.81%) showed a notably lower rate of cell proliferation after PDT treatments compared to that of vesicle-*m*-THPC (31.52 ± 4.06%, $^{+}p < 0.05$) or vesicle-*m*-THPC-FA (31.44 ± 4.45%, $^{a}p < 0.05$) group, indicating efficient nanodisc-based PDT against cancer.

4. DISCUSSION

The dense microenvironment of tumors can cause a poor tumor permeability, followed by a weaker delivery of NPs to the site of action. It was demonstrated that the nanoparticles more effectively penetrated deeply into collagen-rich and/or poorly permeable tumors when their size is smaller than 40 nm.[52] Nanodiscs made of lipid and protein can be obtained with controlled size and composition.[23] Several studies have summarized the advantages of nanodiscs in recent reviews. For example, Numata et al. utilized the phospholipids and the membrane scaffold protein (MSP) to composed nanodisc and containing with palmitoyloleoylphosphatidylglycerol (POPG) lipids per disc demonstrated that antagonist of respiratory syncytial virus (RSV) infection and its inflammatory sequelae both in vitro and in vivo, and showed similar effect in liposome POPG. Although there is a similar antagonist effect of RSV between nanodisc POPC and liposome POPG in this research, the smaller nanodiscs likely provide significant advantages for delivery to the lungs.[53] However, MSP amplified and purified from the prokaryotic system has some drawbacks, such as the degradation of MSP protein by host cell proteases and the codon usage toxicity of the protein to the host.[54] Ng et al. synthesized the sub-40 nm diameter disclike morphology-activatable porphyrin nanodiscs by using complexing apolipoproteins and found that discs turned to vesicle with their size increasing to 100−200 nm in the presence of proteinase K. It is speculated that proteinase K might cleave and dissociate from the apolipoprotein resulting in disc fusion into vesicular structure.[55] The bicellar nanodisc in this study is composed of DPPC, DPPG, DPPG, DHPC, and DSPE-PEG2000 and can successfully encapsulate *m*-THPC. Previously, we have confirmed the stability of self-assembled nanodiscs and liposomes in FBS and HEPES buffer saline, with no structural variation.[22,40] Nanodiscs only turn into vesicles of similar size through incubation at 55 °C or above for several hours, confirmed by TEM, DLS, and SANS.[40] These nanocarriers have long-term stability in aqueous solutions and therefore are suitable as delivery carriers for drugs, vaccines, and genes for a variety of diseases.

We demonstrated that there is a higher cellular uptake and fluorescence intensity in nanodisc-*m*-THPC conjugated without or with FA compared to vesicle-*m*-THPC of the corresponding condition in folate receptor-overexpressed KB cells. The cell viability after photodynamic therapy significantly decreases for nanodiscs compared to vesicles, suggesting that the nanoparticle size and shape affect the rate of penetration through collagen-rich and/or poorly permeable extracellular matrix around the tumors.[52] The nonspherical geometries, e.g., rodlike NPs, have been proved to have deeper penetration in mammary tumors tissues compared to their spherical counterparts with similar average hydrodynamic sizes.[56] Agarwal et al. reported that different sizes of hydrogel nanodiscs and nanorods were fabricated by using jet-and-flash imprint lithography and demonstrated that the nanodiscs were more efficiently incorporated into HeLa cells, mouse bone marrow dendritic cells, and HEK 293 cells compared to the nanorods.[57] It has also been reported that nanodiscs have high diffusion and penetration properties in collagen-rich environment.[55] Presumably, the small dimension along the thickness of the nanodiscs allows for enhanced tumor penetration compared to the symmetric structure of vesicles. The extracellular matrix is expected to have a size-dependent screening effect on the interstitial space of the tumor.

Therapeutic agents containing ligands that bind to overexpressed receptors on the surface of diseased cells have shown preferable uptake by receptor-regulated endocytosis. As folate receptor overexpresses in the apical membrane surface of certain cancer cells, such as ovary, colon, uterus, and kidney,[58] it serves as a promising target for cancer treatment.[59] The inhibited cellular uptake for the folate-conjugated Nile Red- and *m*-THPC-entrapped NPs (Figures 2E−F and 4G−H) after pretreatment of FA supports the aforementioned mechanism. Under physiological conditions, NPs involved in the cells mediated by several pathways, such as macropinocytosis, clathrin-mediated endocytosis, and caveolae-mediated endocytosis.[60] Various factors affect the cellular uptake, including shape, size, and surface charge of NPs.[61,62] It has been reported that the NPs with positive charge are absorbed into cell favorably as they strongly attract the negative-charged phospholipid components of the cell membrane.[61] Dalal et al. synthesized multivalency folate-functionalized nanoparticles and demonstrated that multivalency nanoparticles affected the subcellular trafficking. The high-multivalency NPs trapped in lysosomal and restrict their subcellular targeting by clathrin-mediated endocytosis. The lower-multivalency nanoparticles entered the

DOI: 10.1021/acsami.8b21609
ACS Appl. Mater. Interfaces 2019, 11, 10505−10519

perinuclear region and escaped from the lysosome via caveolae-mediated endocytosis. The multivalency NPs range of 10−40 entered the cell via transition between clathrin- and caveolae-mediated endocytosis.[62] Our research demonstrates that after folate attaches to the receptors located within caveolae, it is internalized through the endocytotic pathway. As the endosome is acidic, the folate can dissociate from the receptor and release the drug.[50] The fact that the nanodiscs or vesicles conjugated with folate had lower colocalization percentage with lysosome in KB cells shows a different pathway from the non-folate-conjugated bicelles and vesicles or free *m*-THPC, which follow caveolae-mediated uptake into the perinuclear region and clathrin-regulated endocytosis to the lysosomes.

Folate receptors, however, are also expressed with several health in vivo tissues, such as choroid plexus, lungs, or the proximal tubules of kidney.[63] It has been reported that the folate receptors are localized on the apical membrane of polarized epithelial cells, indicating that the folate receptor expressed facing the lumen of the proximal tubules of the kidney. For choroid plexus, the folate receptors are expressed toward the cerebrospinal fluid. These healthy tissues may be subjected to potential toxicities by folate-targeting therapy. However, the folate−drug conjugates seemed not to show any adverse effect.[64] In the healthy tissues, the FR is not accessible to the blood stream since they are localized in the apical surface of the polarized epithelium.[65] Also, the different vasculature between the healthy and cancerous tissues, which contains defects in the size range of hundreds of nanometers in contrast to the pore size of a few nanometers in the healthy tissue (i.e., EPR effect), would enhance the success. Hence, it is expected the nanocarriers with folate would show higher uptake by cancer cells whose surface is overexpressed with the folate receptor.[27,34] An example can be found in a study in EMT6 tumor animal model treated with lipid-shell and polymer-core nanoparticles and targeted delivery of paclitaxel modification with folate, which displayed significant antitumor effect and lower toxicity (low weight loss) compared to Taxol.[66] The folate-targeted vinca alkaloid conjugates-EC145 applied in KB tumor xenograft animal model also showed excellent antitumor effect. For the above reasons, folate is one of the appropriate choices for nanotechnology-based cancer treatment.

It is noteworthy that all lipids (PEG2000-DSPE, DPPG DPPC, and DHPC) that constitute the nanodiscs or vesicles are FDA-approved. Currently, the liposome products, such as Doxil (HSPC, Cholesterol, PEG2000-DSPE, clinical products), Depocyt (DOPC, DPPG, cholesterol and triolein, clinical products),[67] ThermoDox (DPPC, myristoyl stearyl phosphatidylcholine, and DSPE-*N*-[amino(poly(ethylene glycol))-2000], Phase III),[68] are either in clinical trials or approved and used in the clinic. These lipids are similar to the formulation in this research.

Based on the in vivo experiment, the results indicate that the nanodiscs are even more efficient than the optimized vesicles in terms of NP size (∼50 nm) and surface ligand density.[32,41] Interestingly, a recent study on modeling for in vitro and ex vivo experiments demonstrated that discoidal geometries possessed the most favorable margination dynamics in the body.[69] It has been recently shown that discoidal nanoparticles show particular movement dynamics that favor the interaction with vessel wall more than spherical particles.[12] Likewise, NPs' geometries affect hemorheological dynamics, cellular uptake, and in vivo fate. Therefore, the observed differences between biological responses to our various samples can be explained by the aforementioned reasons. However, to the best of our knowledge, the discoidal shape has not been studied in a fair comparison with another shape to be optimized for tumor targeting purposes. Hence, the current study provides the correlation of shape with cellular uptake under the identical chemical composition, suggesting that disc is a promising shape for the next-generation nanocarriers. The shift from conventional paradigms of EPR, NP chemistry, and size to other parameters such as shape can open a new pathway into more successful cancer therapies.

5. CONCLUSIONS

Both in vitro and in vivo results indicate the impacts of morphology, and ligand-targeting nanoparticles enhance the NP accumulation in cancer cells. The toxicity of the folate and nonfolate NPs are insignificant to KB cells. The in vitro study further shows that the folate targeting is efficacious for internalization of KB cells. Regarding morphological dependence, we have demonstrated that even the optimal-size vesicles show lower cellular uptake than the nanodiscs do. The experimental outcomes of in vitro cellular uptake and in vivo tumor accumulation suggest that folate disc > folate vesicle > nonfolate disc > nonfolate vesicle. The size of both vesicles and nanodiscs are in the range of sub-100 nm and, most importantly, they are made from biocompatible molecules with identical chemical compositions to minimize the bias in chemistry. The nanodisc platform can be used for encapsulating hydrophobic therapeutics. The in vivo outcome indicates that lipid nanodisc-*m*-THPC-FA is an efficacious nanocarrier for potential PDT cancer treatment. Last but not least, the most attractive feature of this system is the robust formation of these uniform self-assemblies, making scalable manufacturing feasible as well as its adaptability for ligand/surface modification, providing great potential for future theranostic applications.

■ ASSOCIATED CONTENT

Supporting Information

The Supporting Information is available free of charge on the ACS Publications website at DOI: 10.1021/acsami.8b21609.

Cytotoxicity assay of the nanocarriers (Section S1); photodynamic active nanoparticles characterization (Section S2); SAXS analysis (a) core−three-shell spherical model and (b) core−shell discoidal model (Section S3) (PDF)

■ AUTHOR INFORMATION

Corresponding Authors

*E-mail: pslai@email.nchu.edu.tw (P.-S.L.).
*E-mail: Mu-Ping.Nieh@UConn.edu (M.-P.N.).

Author Contributions

⊥A.T.R., C.-W.C., and W.A. contributed equally to this work.

Notes

The authors declare no competing financial interest.

■ ACKNOWLEDGMENTS

The authors acknowledge the National Science Foundation (NSF) for the financial support (CBET 1605971) and Ministry of Science and Technology of Taiwan (106-2113-M-005-014-MY3). The SAXS instrument was partially funded through NSF-MRI (DMR 1228817). The authors thank Liam Evans and Kimberly Nguyen for their technical assistance.

DOI: 10.1021/acsami.8b21609
ACS Appl. Mater. Interfaces 2019, 11, 10505−10519

REFERENCES

(1) Chithrani, B. D.; Ghazani, A. A.; Chan, W. C. Determining the Size and Shape Dependence of Gold Nanoparticle Uptake into Mammalian Cells. *Nano Lett.* **2006**, *6*, 662−668.

(2) Albanese, A.; Tang, P. S.; Chan, W. C. The Effect of Nanoparticle Size, Shape, and Surface Chemistry on Biological Systems. *Annu. Rev. Biomed. Eng.* **2012**, *14*, 1−16.

(3) Wang, Y.; Miao, L.; Satterlee, A.; Huang, L. Delivery of Oligonucleotides with Lipid Nanoparticles. *Adv. Drug Delivery Rev.* **2015**, *87*, 68−80.

(4) Torchilin, V. P. Recent Advances with Liposomes as Pharmaceutical Carriers. *Nat. Rev. Drug Discovery* **2005**, *4*, 145−160.

(5) Dreher, M. R.; Liu, W.; Michelich, C. R.; Dewhirst, M. W.; Yuan, F.; Chilkoti, A. Tumor Vascular Permeability, Accumulation, and Penetration of Macromolecular Drug Carriers. *J. Natl. Cancer Inst.* **2006**, *98*, 335−344.

(6) Hsu, H. J.; Bugno, J.; Lee, Sr.; Hong, S. Dendrimer-Based Nanocarriers: A Versatile Platform for Drug Delivery. *Wiley Interdiscip. Rev.: Nanomed. Nanobiotechnol.* **2017**, *9*, No. e1409.

(7) Lai, S.-M.; Chiou, Y.-C.; Chen, G.-F.; Liao, M.-Y.; Tzen, J. T.; Lai, P. S. Enhanced Nuclear Localization of Photosensitizer Using Artificial Oil Bodies for Photodynamic Therapy. *Smart Sci.* **2016**, *4*, 167−172.

(8) Patri, A. K.; Majoros, I. J.; Baker, J. R. Dendritic Polymer Macromolecular Carriers for Drug Delivery. *Curr. Opin. Chem. Biol.* **2002**, *6*, 466−471.

(9) Ashley, C. E.; Carnes, E. C.; Phillips, G. K.; Padilla, D.; Durfee, P. N.; Brown, P. A.; Hanna, T. N.; Liu, J.; Phillips, B.; Carter, M. B. The Targeted Delivery of Multicomponent Cargos to Cancer Cells by Nanoporous Particle-Supported Lipid Bilayers. *Nat. Mater.* **2011**, *10*, No. 389.

(10) Alexis, F.; Pridgen, E.; Molnar, L. K.; Farokhzad, O. C. Factors Affecting the Clearance and Biodistribution of Polymeric Nanoparticles. *Mol. Pharm.* **2008**, *5*, 505−515.

(11) Danhier, F. To Exploit the Tumor Microenvironment: Since the Epr Effect Fails in the Clinic, What Is the Future of Nanomedicine? *J. Controlled Release* **2016**, *244*, 108−121.

(12) Blanco, E.; Shen, H.; Ferrari, M. Principles of Nanoparticle Design for Overcoming Biological Barriers to Drug Delivery. *Nat. Biotechnol.* **2015**, *33*, 941−951.

(13) Agarwal, R.; Singh, V.; Jurney, P.; Shi, L.; Sreenivasan, S.; Roy, K. Mammalian Cells Preferentially Internalize Hydrogel Nanodiscs over Nanorods and Use Shape-Specific Uptake Mechanisms. *Proc. Natl. Acad. Sci. U.S.A.* **2013**, *110*, 17247−17252.

(14) Truong, N. P.; Whittaker, M. R.; Mak, C. W.; Davis, T. P. The Importance of Nanoparticle Shape in Cancer Drug Delivery. *Expert Opin. Drug Delivery* **2015**, *12*, 129−142.

(15) Nagahama, K.; Kawano, D.; Oyama, N.; Takemoto, A.; Kumano, T.; Kawakami, J. Self-Assembling Polymer Micelle/Clay Nanodisk/Doxorubicin Hybrid Injectable Gels for Safe and Efficient Focal Treatment of Cancer. *Biomacromolecules* **2015**, *16*, 880−889.

(16) Sun, W.; Parowatkin, M.; Steffen, W.; Butt, H. J.; Mailänder, V.; Wu, S. Ruthenium-Containing Block Copolymer Assemblies: Red-Light-Responsive Metallopolymers with Tunable Nanostructures for Enhanced Cellular Uptake and Anticancer Phototherapy. *Adv. Healthcare Mater.* **2016**, *5*, 467−473.

(17) Sun, W.; Wen, Y.; Thiramanas, R.; Chen, M.; Han, J.; Gong, N.; Wagner, M.; Jiang, S.; Meijer, M. S.; Bonnet, S.; et al. Red-Light-Controlled Release of Drug−Ru Complex Conjugates from Metallopolymer Micelles for Phototherapy in Hypoxic Tumor Environments. *Adv. Funct. Mater.* **2018**, *28*, No. 1804227.

(18) Ernsting, M. J.; Murakami, M.; Roy, A.; Li, S. D. Factors Controlling the Pharmacokinetics, Biodistribution and Intratumoral Penetration of Nanoparticles. *J. Controlled Release* **2013**, *172*, 782−794.

(19) Tan, J.; Shah, S.; Thomas, A.; Ou-Yang, H. D.; Liu, Y. The Influence of Size, Shape and Vessel Geometry on Nanoparticle Distribution. *Microfluid. Nanofluid.* **2013**, *14*, 77−87.

(20) Gratton, S. E.; Ropp, P. A.; Pohlhaus, P. D.; Luft, J. C.; Madden, V. J.; Napier, M. E.; DeSimone, J. M. The Effect of Particle Design on Cellular Internalization Pathways. *Proc. Natl. Acad. Sci. U.S.A.* **2008**, *105*, 11613−11618.

(21) Nieh, M. P.; Kucerka, N.; Katsaras, J. Spontaneously Formed Unilamellar Vesicles. *Methods Enzymol.* **2009**, *465*, 3−20.

(22) Aresh, W.; Liu, Y.; Sine, J.; Thayer, D.; Puri, A.; Huang, Y.; Wang, Y.; Nieh, M.-P. The Morphology of Self-Assembled Lipid-Based Nanoparticles Affects Their Uptake by Cancer Cells. *J. Biomed. Nanotechnol.* **2016**, *12*, 1852−1863.

(23) Liu, Y.; Xia, Y.; Rad, A. T.; Aresh, W.; Nieh, M.-P. Stable Discoidal Bicelles: A Platform of Lipid Nanocarriers for Cellular Delivery. *Liposomes*; Humana Press: NY, 2017; pp 273−282.

(24) Nieh, M. P.; Dolinar, P.; Kucerka, N.; Kline, S. R.; Debeer-Schmitt, L. M.; Littrell, K. C.; Katsaras, J. Formation of Kinetically Trapped Nanoscopic Unilamellar Vesicles from Metastable Nanodiscs. *Langmuir* **2011**, *27*, 14308−14316.

(25) Nieh, M. P.; Raghunathan, V. A.; Kline, S. R.; Harroun, T. A.; Huang, C. Y.; Pencer, J.; Katsaras, J. Spontaneously Formed Unilamellar Vesicles with Path-Dependent Size Distribution. *Langmuir* **2005**, *21*, 6656−6661.

(26) Zhang, Z.; Jia, J.; Lai, Y.; Ma, Y.; Weng, J.; Sun, L. Conjugating Folic Acid to Gold Nanoparticles through Glutathione for Targeting and Detecting Cancer Cells. *Bioorg. Med. Chem.* **2010**, *18*, 5528−5534.

(27) Zwicke, G. L.; Mansoori, G. A.; Jeffery, C. J. Utilizing the Folate Receptor for Active Targeting of Cancer Nanotherapeutics. *Nano Rev.* **2012**, *3*, No. 18496.

(28) Müller, C.; Schibli, R. Folic Acid Conjugates for Nuclear Imaging of Folate Receptor−Positive Cancer. *J. Nucl. Med.* **2011**, *52*, 1−4.

(29) Vlashi, E.; Kelderhouse, L. E.; Sturgis, J. E.; Low, P. S. Effect of Folate-Targeted Nanoparticle Size on Their Rates of Penetration into Solid Tumors. *ACS Nano* **2013**, *7*, 8573−8582.

(30) Parker, N.; Turk, M. J.; Westrick, E.; Lewis, J. D.; Low, P. S.; Leamon, C. P. Folate Receptor Expression in Carcinomas and Normal Tissues Determined by a Quantitative Radioligand Binding Assay. *Anal. Biochem.* **2005**, *338*, 284−293.

(31) Mahabir, S.; Wan, W.; Katsaras, J.; Nieh, M.-P. Effects of Charge Density and Thermal History on the Morphologies of Spontaneously Formed Unilamellar Vesicles. *J. Phys. Chem. B* **2010**, *114*, 5729−5735.

(32) Arvizo, R. R.; Miranda, O. R.; Thompson, M. A.; Pabelick, C. M.; Bhattacharya, R.; Robertson, J. D.; Rotello, V. M.; Prakash, Y.; Mukherjee, P. Effect of Nanoparticle Surface Charge at the Plasma Membrane and Beyond. *Nano Lett.* **2010**, *10*, 2543−2548.

(33) Shieh, M.-J.; Peng, C.-L.; Chiang, W.-L.; Wang, C.-H.; Hsu, C.-Y.; Wang, S.-J. J.; Lai, P.-S. Reduced Skin Photosensitivity with Meta-Tetra (Hydroxyphenyl) Chlorin-Loaded Micelles Based on a Poly (2-Ethyl-2-Oxazoline)-B-Poly (D, L-Lactide) Diblock Copolymer in Vivo. *Mol. Pharm.* **2010**, *7*, 1244−1253.

(34) Syu, W. J.; Yu, H. P.; Hsu, C. Y.; Rajan, Y. C.; Hsu, Y. H.; Chang, Y. C.; Hsieh, W. Y.; Wang, C. H.; Lai, P. S. Improved Photodynamic Cancer Treatment by Folate-Conjugated Polymeric Micelles in a Kb Xenografted Animal Model. *Small* **2012**, *8*, 2060−2069.

(35) Horlings, R. K.; Terra, J. B.; Witjes, M. J. Mthpc Mediated, Systemic Photodynamic Therapy (Pdt) for Nonmelanoma Skin Cancers: Case and Literature Review. *Lasers Surg. Med.* **2015**, *47*, 779−787.

(36) Laad, P.; Shete, G.; Modi, S. R.; Bansal, A. K. Differential Surface Properties of Commercial Crystalline Telmisartan Samples. *Eur. J. Pharm. Sci.* **2013**, *49*, 109−116.

(37) Testa, B.; Carrupt, P.-A.; Gaillard, P.; Billois, F.; Weber, P. Lipophilicity in Molecular Modeling. *Pharm. Res.* **1996**, *13*, 335−343.

(38) *Molecular Surface Lipophilicity Potential Calculator of Molinspiration Property Calculation Service*, 2018. www.molinspiration.com.

(39) Gomer, C. J.; Ferrario, A. Tissue Distribution and Photosensitizing Properties of Mono-L-Aspartyl Chlorin E6 in a Mouse Tumor Model. *Cancer Res* **1990**, *50*, 3985−3990.

(40) Liu, Y.; Li, M.; Yang, Y.; Xia, Y.; Nieh, M.-P. The Effects of Temperature, Salinity, Concentration and Pegylated Lipid on the Spontaneous Nanostructures of Bicellar Mixtures. *Biochim. Biophys. Acta, Biomembr.* **2014**, *1838*, 1871−1880.

DOI: 10.1021/acsami.8b21609
ACS Appl. Mater. Interfaces 2019, 11, 10505−10519

(41) Xiao, K.; Li, Y.; Luo, J.; Lee, J. S.; Xiao, W.; Gonik, A. M.; Agarwal, R. G.; Lam, K. S. The Effect of Surface Charge on in Vivo Biodistribution of Peg-Oligocholic Acid Based Micellar Nanoparticles. *Biomaterials* **2011**, *32*, 3435−3446.
(42) Yuan, H.; Li, J.; Bao, G.; Zhang, S. Variable Nanoparticle-Cell Adhesion Strength Regulates Cellular Uptake. *Phys. Rev. Lett.* **2010**, *105*, No. 138101.
(43) Barua, S.; Yoo, J.-W.; Kolhar, P.; Wakankar, A.; Gokarn, Y. R.; Mitragotri, S. Particle Shape Enhances Specificity of Antibody-Displaying Nanoparticles. *Proc. Natl. Acad. Sci. U.S.A.* **2013**, *110*, 3270−3275.
(44) Gabizon, A.; Shmeeda, H.; Horowitz, A. T.; Zalipsky, S. Tumor Cell Targeting of Liposome-Entrapped Drugs with Phospholipid-Anchored Folic Acid-Peg Conjugates. *Adv. Drug Delivery Rev.* **2004**, *56*, 1177−1192.
(45) Decuzzi, P.; Pasqualini, R.; Arap, W.; Ferrari, M. Intravascular Delivery of Particulate Systems: Does Geometry Really Matter? *Pharm. Res.* **2009**, *26*, 235−243.
(46) Sessa, G.; Weissmann, G. Phospholipid Spherules (Liposomes) as a Model for Biological Membranes. *J. Lipid Res.* **1968**, *9*, 310−318.
(47) Leamon, C. P.; Jackman, A. L. Chapter 7 Exploitation of the Folate Receptor in the Management of Cancer and Inflammatory Disease. *Vitam. Horm.* **2008**, *79*, 203−233.
(48) Zhang, L.; Zhu, D.; Dong, X.; Sun, H.; Song, C.; Wang, C.; Kong, D. Folate-Modified Lipid-Polymer Hybrid Nanoparticles for Targeted Paclitaxel Delivery. *Int. J. Nanomed.* **2015**, *10*, 2101−2114.
(49) Leamon, C. P.; Reddy, J. A.; Vlahov, I. R.; Westrick, E.; Parker, N.; Nicoson, J. S.; Vetzel, M. Comparative Preclinical Activity of the Folate-Targeted Vinca Alkaloid Conjugates Ec140 and Ec145. *Int. J. Cancer* **2007**, *121*, 1585−1592.
(50) Mansoori, G. A.; Brandenburg, K. S.; Shakeri-Zadeh, A. A Comparative Study of Two Folate-Conjugated Gold Nanoparticles for Cancer Nanotechnology Applications. *Cancers* **2010**, *2*, No. 1911.
(51) Cuong, N.-V.; Li, Y.-L.; Hsieh, M.-F. Targeted Delivery of Doxorubicin to Human Breast Cancers by Folate-Decorated Star-Shaped Peg-Pcl Micelle. *J. Mater. Chem.* **2012**, *22*, 1006−1020.
(52) Cabral, H.; Matsumoto, Y.; Mizuno, K.; Chen, Q.; Murakami, M.; Kimura, M.; Terada, Y.; Kano, M. R.; Miyazono, K.; Uesaka, M.; Nishiyama, N.; Kataoka, K. Accumulation of Sub-100 nm Polymeric Micelles in Poorly Permeable Tumours Depends on Size. *Nat. Nanotechnol.* **2011**, *6*, 815−823.
(53) Numata, M.; Grinkova, Y. V.; Mitchell, J. R.; Chu, H. W.; Sligar, S. G.; Voelker, D. R. Nanodiscs as a Therapeutic Delivery Agent: Inhibition of Respiratory Syncytial Virus Infection in the Lung. *Int. J. Nanomed.* **2013**, *8*, 1417−1427.
(54) Rosano, G. L.; Ceccarelli, E. A. Recombinant Protein Expression in Escherichia Coli: Advances and Challenges. *Front. Microbiol.* **2014**, *5*, No. 172.
(55) Ng, K. K.; Lovell, J. F.; Vedadi, A.; Hajian, T.; Zheng, G. Self-Assembled Porphyrin Nanodiscs with Structure-Dependent Activation for Phototherapy and Photodiagnostic Applications. *ACS Nano* **2013**, *7*, 3484−3490.
(56) Chauhan, V. P.; Popovic, Z.; Chen, O.; Cui, J.; Fukumura, D.; Bawendi, M. G.; Jain, R. K. Fluorescent Nanorods and Nanospheres for Real-Time in Vivo Probing of Nanoparticle Shape-Dependent Tumor Penetration. *Angew. Chem., Int. Ed.* **2011**, *50*, 11417−11420.
(57) Agarwal, R.; Singh, V.; Jurney, P.; Shi, L.; Sreenivasan, S. V.; Roy, K. Mammalian Cells Preferentially Internalize Hydrogel Nanodiscs over Nanorods and Use Shape-Specific Uptake Mechanisms. *Proc. Natl. Acad. Sci. U.S.A.* **2013**, *110*, 17247−17252.
(58) Shi, H.; Guo, J.; Li, C.; Wang, Z. A Current Review of Folate Receptor Alpha as a Potential Tumor Target in Non-Small-Cell Lung Cancer. *Drug Des., Dev. Ther.* **2015**, *9*, 4989−4996.
(59) Kukowska-Latallo, J. F.; Candido, K. A.; Cao, Z.; Nigavekar, S. S.; Majoros, I. J.; Thomas, T. P.; Balogh, L. P.; Khan, M. K.; Baker, J. R., Jr. Nanoparticle Targeting of Anticancer Drug Improves Therapeutic Response in Animal Model of Human Epithelial Cancer. *Cancer Res.* **2005**, *65*, 5317−5324.
(60) Kumari, S.; Mg, S.; Mayor, S. Endocytosis Unplugged: Multiple Ways to Enter the Cell. *Cell Res.* **2010**, *20*, 256−275.
(61) Verma, A.; Stellacci, F. Effect of Surface Properties on Nanoparticle-Cell Interactions. *Small* **2010**, *6*, 12−21.
(62) Dalal, C.; Saha, A.; Jana, N. R. Nanoparticle Multivalency Directed Shifting of Cellular Uptake Mechanism. *J. Phys. Chem. C* **2016**, *120*, 6778−6786.
(63) Birn, H.; Selhub, J.; Christensen, E. I. Internalization and Intracellular Transport of Folate-Binding Protein in Rat Kidney Proximal Tubule. *Am. J. Physiol.* **1993**, *264*, C302−C310.
(64) Leamon, C. P.; Reddy, J. A. Folate-Targeted Chemotherapy. *Adv. Drug Delivery Rev.* **2004**, *56*, 1127−1141.
(65) Fasehee, H.; Dinarvand, R.; Ghavamzadeh, A.; Esfandyari-Manesh, M.; Moradian, H.; Faghihi, S.; Ghaffari, S. H. Delivery of Disulfiram into Breast Cancer Cells Using Folate-Receptor-Targeted Plga-Peg Nanoparticles: In Vitro and in Vivo Investigations. *J. Nanobiotechnol.* **2016**, *14*, No. 32.
(66) Zhang, L.; Zhu, D.; Dong, X.; Sun, H.; Song, C.; Wang, C.; Kong, D. Folate-Modified Lipid−Polymer Hybrid Nanoparticles for Targeted Paclitaxel Delivery. *Int. J. Nanomed.* **2015**, *10*, No. 2101.
(67) Glantz, M. J.; Jaeckle, K. A.; Chamberlain, M. C.; Phuphanich, S.; Recht, L.; Swinnen, L. J.; Maria, B.; LaFollette, S.; Schumann, G. B.; Cole, B. F.; Howell, S. B. A Randomized Controlled Trial Comparing Intrathecal Sustained-Release Cytarabine (Depocyt) to Intrathecal Methotrexate in Patients with Neoplastic Meningitis from Solid Tumors. *Clin. Cancer Res.* **1999**, *5*, 3394−3402.
(68) Chen, J.; He, C. Q.; Lin, A. H.; Gu, W.; Chen, Z. P.; Li, W.; Cai, B. C. Thermosensitive Liposomes with Higher Phase Transition Temperature for Targeted Drug Delivery to Tumor. *Int. J. Pharm.* **2014**, *475*, 408−415.
(69) Lee, H.; Fonge, H.; Hoang, B.; Reilly, R. M.; Allen, C. The Effects of Particle Size and Molecular Targeting on the Intratumoral and Subcellular Distribution of Polymeric Nanoparticles. *Mol. Pharm.* **2010**, *7*, 1195−1208.

DOI: 10.1021/acsami.8b21609
ACS Appl. Mater. Interfaces 2019, 11, 10505−10519